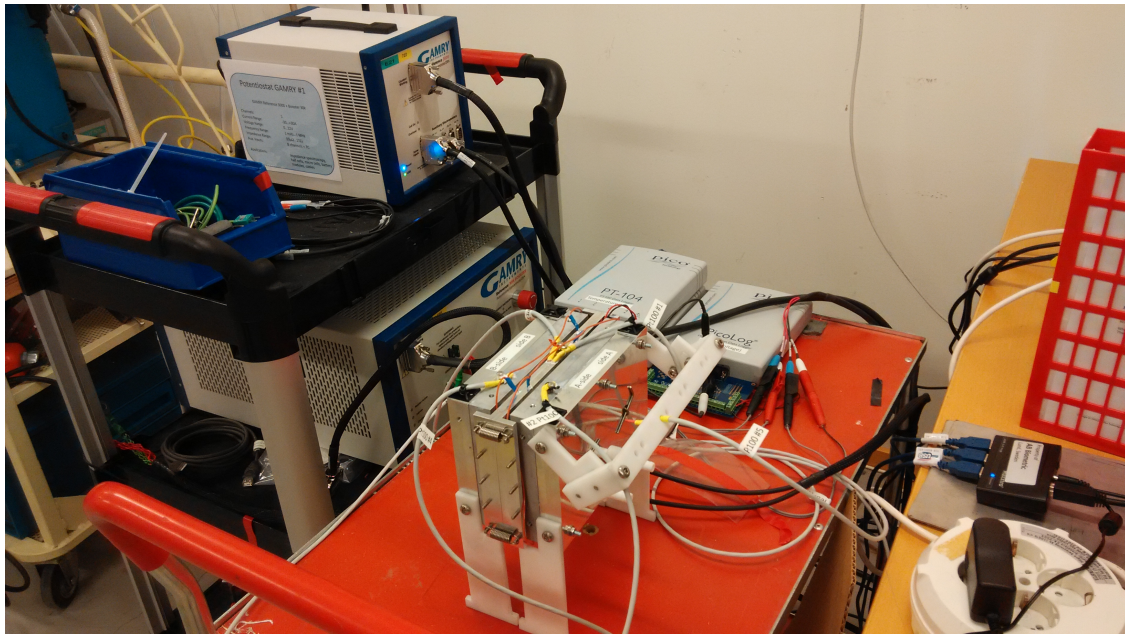




CHALMERS
UNIVERSITY OF TECHNOLOGY



Experimental Characterization of Li-ion Battery cells for Thermal Management in Heavy Duty Hybrid Applications

Master of Science Thesis

Anton Lidbeck
Kazim Raza Syed

Department of Energy and Environment - Division of Electric Power Engineering
CHALMERS UNIVERSITY OF TECHNOLOGY
Gothenburg, Sweden 2017

MASTER'S THESIS 2017

Experimental Characterization of Li-ion Battery cells for Thermal Management in Heavy Duty Hybrid Applications

Anton Lidbeck
Kazim Raza Syed



CHALMERS
UNIVERSITY OF TECHNOLOGY

Department of Energy and Environment
Division of Electric Power Engineering
CHALMERS UNIVERSITY OF TECHNOLOGY
Gothenburg, Sweden 2017

Experimental Characterization of Li-ion Battery cells for Thermal Management in Heavy Duty Hybrid Applications

© Anton Lidbeck
Kazim Raza Syed, 2017.

Supervisor: Jens Groot, Volvo Group Trucks Technology
Examiner: Torbjörn Thiringer, Chalmers

Master's Thesis 2017
Department of Energy and Environment
Division of Electric Power Engineering
Chalmers University of Technology
SE-412 96 Gothenburg
Telephone +46 31 772 1000

Cover: Photo of the measurement setup in the battery lab at Volvo GTT.

Typeset in L^AT_EX
Printed by Reproservice
Gothenburg, Sweden 2017

Experimental Characterization of Li-ion Battery cells for Thermal Management in Heavy Duty Hybrid Applications
Anton Lidbeck & Kazim Raza Syed
Department of Energy and Environment
Chalmers University of Technology

Abstract

The performance and lifetime of lithium ion (Li-ion) batteries are highly dependent on the internal operating temperature which makes thermal characterization of battery cells necessary. Therefore, the main focus of this thesis work was to characterize pouch and prismatic Li-ion cells by designing and conducting experiments to measure thermal parameters. The specific heat capacity was quantified as well as the heat conductivity in three dimensions. In addition, the heat generation from the cells was measured for different load cycles. Subsequently, the determined thermal parameters were inputs in a simulation model to determine the internal peak temperature of the cell during different load cycles.

The experiments were carried out by using a custom-designed isothermal heat conduction calorimeter (IHC). This calorimeter was modified for measurement of individual thermal parameters. The modified setup was verified using available sample materials and subsequently applied for measurements on the Li-ion cells. The heat generated within the cells was measured for constant current rates and a dynamic operation cycle.

The through-plane thermal conductivity for the provided pouch cell was measured to be lower than the in-plane ($0.7 \text{ W m}^{-1} \text{ K}^{-1}$ compared to $20\text{-}30 \text{ W m}^{-1} \text{ K}^{-1}$). In addition, the specific heat capacity was measured to be $\approx 1100 \text{ J kg}^{-1} \text{ K}^{-1}$ for a pouch cell and a prismatic cell. Lastly, the heat generated by the cells was measured between 10 mW to 30 W .

To conclude, the heat generation and specific heat capacity was measured successfully for both the pouch and prismatic Li-ion cell. The methods for thermal conductivity in through-plane and in-plane were utilized for the pouch cell. However, the proposed methods for thermal conductivities were found to be inapplicable for prismatic cells due to the conduction through the aluminum casing. Nevertheless, this opens up opportunities within the thermal characterization of Li-ion batteries.

Keywords: Isothermal, Calorimeter, Specific heat capacity, Thermal conductivity, Li-ion, Battery, SOC, Pouch cell, Prismatic cell, Tian correction.

"...it is so difficult to trap heat!" - Authors

Acknowledgements

First and foremost we would like to thank our supervisor Jens Groot for his support and guidance throughout all the ups and downs in the thesis work. We would also like to thank Torbjörn Thiringer, Istaq Ahmed and Evelina Wikner for very interesting discussions and feedback during our meetings. In addition, Joachim Claesson gave us valuable feedback on our work.

We are also very thankful for all the resources made available to us at Volvo GTT in the battery lab and the mechanical workshops. Mikael Ohlsson and Roald Karlsson should have a special mention for their helpfulness in the workshops and the battery lab.

Finally, we want to give our gratitude to the Volvo GTT department for giving us this opportunity to conduct the thesis work. This acknowledgement will be incomplete without thanking the talented people in the department who were always eager to discuss issues at 'fika-sessions'.

Anton Lidbeck & Kazim Raza Syed, Gothenburg, 2017

Contents

1	Introduction	1
1.1	Background	1
1.2	Previous work	2
1.3	Purpose	4
1.4	Scope	5
1.5	Environmental & ethical aspects	6
2	Technical background	7
2.1	Li-ion cells	7
2.1.1	Cell designs	9
2.1.2	Equivalent circuit battery model	11
2.2	Heat transfer	11
2.3	Calorimeters and calorimetry	12
2.3.1	Isothermal heat-conduction calorimeter	13
2.3.2	Calibration of IHC	14
2.3.3	Thermal output and dynamic correction	15
3	Experimental setup	19
3.1	General setup	19
3.2	Measurement equipment	20
3.3	Calibration	22
3.3.1	Calorimeter setup	22
3.3.2	Calibration heater	23
3.3.3	Calibration constant	24
3.3.4	Validation of calibration constant	25
3.4	Temperature sensors	26
4	Measurement of through-plane thermal conductivity	29
4.1	Method development	29
4.2	Validation	30
5	Measurement of in-plane thermal conductivity	33
5.1	Method development	33
5.1.1	Heater configuration	34
5.1.2	Heat flow sensor configuration	35
5.2	Fixed setup	36
5.3	Modular setup	37
6	Measurement of specific heat capacity	41
6.1	Method development	41
6.1.1	Dynamic method	41
6.1.2	Absorbed Heat Method	42
6.2	Validation	44

7	Battery cell measurements	47
7.1	Through-plane thermal conductivity	47
7.2	In-plane thermal conductivity	48
7.3	Specific heat capacity	50
7.4	Heat generation - Pouch cell	51
7.5	Heat generation - Prismatic cell	55
7.6	Simulation model	58
7.6.1	Load cycle - 1.67C discharge and charge	60
7.6.2	Load cycle - dynamic	60
8	Conclusion	63
8.1	Future work	64
	Bibliography	67
A	Appendix 1	I
A.1	Measurement uncertainty - calibration coefficient	I
A.2	Measurement uncertainty - through-plane thermal conductivity	III
A.3	Measurement uncertainty - in-plane thermal conductivity	IV
A.4	Measurement uncertainty - specific heat capacity	VI

Glossary

ARC	Accelerated Rate Calorimeter
CAD	Computer Aided Design
DC	Direct current
EV	Electric Vehicle
HDPE	High Density Polyethylene
HEV	Hybrid Electric Vehicle
ICE	Internal Combustion Engine
IHC	Isothermal Heat conduction Calorimeter
LFP	Lithium iron Phosphate
LMO	Lithium Manganese Oxide
LTO	Lithium-titanate
NMC	Lithium Nickel Cobalt Manganese Oxide
OCV	Open Circuit Voltage
SOC	State of Charge

1

Introduction

The environmental aspects have become vital components in numerous research areas during the last decade, especially in the automotive industry [1]. Due to carbon dioxide emissions from internal combustion engines (ICEs), the electric vehicles (EVs) have gained popularity [2].

A bottleneck for the electric vehicles has been the energy storage since the petrol used in ICEs has superior energy density compared to batteries. However, during the last decade different lithium-ion (Li-ion) battery types have gained ground in the market [2]. The research within the area of Li-ion technology has increased in proportion to the usage. The performance and lifetime of Li-ion batteries are highly dependent on the operating temperature which makes thermal management of battery packs necessary during operation.

1.1 Background

The heat generation or energy loss within the battery is dependent on the charge and discharge rates. This generated heat, if not dissipated via a cooling system, will lead to high internal battery temperatures [3]. Thus, measurement of heat generated from batteries by using experimental techniques or electro-thermal models has been an area of interest for electric vehicle (EV) manufacturers. This information is needed for sizing the capacity of the battery pack cooling system in the vehicle. The intent is to keep the system weight as low as possible for prolonging the vehicle range per charge. However, all batteries generates different thermal heat losses for operating charging and discharging rates. This can mainly be attributed to individual manufacturer's approach to cell component material, geometry and packaging strategies [3]. Moreover, opening the battery casing to investigate the internal structure and composition of a cell can be impractical and unsafe.

In addition, the control of many cooling systems is based on measurements of cell surface temperature which may not be a true indicator of the cell internal temperature [4]. A high internal temperature can lead to decreased cell life time and in more severe cases, even lead to thermal hazards.

Therefore, to ensure adequate cooling and prolong the life of batteries, thermal properties are required by electric vehicle manufacturers. These properties are used in designing battery thermal models which can be implemented to evaluate the battery internal temperatures during operation cycles and optimize the cooling system.

1.2 Previous work

In this section, the work carried out in literature on thermal characterization of Li-ion cells is summarized. The list of work highlights the missing information required to tackle the issue of battery thermal parameter evaluation. Finally, the motivation for this thesis work is presented.

Vertiz et.al. have studied the thermal characterization of a large size li-ion pouch cell based on a 1D electro-thermal model [5]. It is stated that the thermal management is established by the *intrinsic thermal properties* like specific heat capacity and thermal conductivity and the *heat generation electro-thermal parameters* like open circuit voltage (OCV), internal resistance and entropic factor (described more in Chapter 2). The experimental results were compared with the calculated values using the knowledge of its exact compound specifications and lengths. It was shown that the measured and calculated values for the specific heat capacity were similar when using an Accelerating Rate Calorimeter (ARC) which is a type of adiabatic calorimeter (described in section 2.3.1). For the thermal conductivity a standardized method called guarded hot plate was utilized which resulted in a value three times lower for the measurement compared to the calculated theoretical value. This highlighted the error in their theoretical model for calculating thermal conductivity, which did not account for thermal contact between internal solid layers. However, this experimental method was not applicable for measurement of in-plane thermal conductivity. As it can be dangerous to open a cell it is of great interest to find precise measurement methods to quantify the thermal properties.

Chen et.al. [6] used an isothermal heat conduction calorimeter (IHC) to measure the heat generation in prismatic Li-ion cells ($A123LiFePO_4$). The aim was to understand the battery characteristics in the best way possible to be able to develop good thermal management systems for EVs. The calorimeter was designed for prismatic batteries which tend to loose more heat from front and back faces as they have higher surface area to thickness ratio. The prismatic battery was placed in direct contact between two slabs of high density polyethylene (HDPE), both of which are five times the thickness of battery. This assembly was placed between two aluminum slabs for strength and placed in an isothermal bath of 50-50 mixture of ethylene glycol-water. They placed two high accuracy thermocouples, one in each HDPE slab and approximately at a depth equal to the center of the battery. Two additional thermocouples were placed over each battery surface. The idea behind this setup was to estimate the heat generated in the batteries from the temperature measurements, assuming one dimensional heat transfer in the HDPE slab. The electrodes of the battery were kept above the liquid bath at all times during the experiment. The results had an

inaccuracy in measurement of the heat generation against a known input heat from heaters of approximately 20 % for the temperature range -10 to 40 °C in this setup. In addition to the relatively low accuracy of the heat measurement, the setup failed to measure any thermal parameter such as specific heat capacity or thermal conductivity of the Li-ion cell. Hence, the measured heat generation can only be used to estimate the capacity of cooling system and not estimate the internal temperatures of the battery.

Viswakarma & Jain [7] carried out experimental measurement of in-plane thermal conductivity and heat capacity of separator sheets in Li-ion cells using the transient direct current (DC) heating method. The separator sheet is used in Li-ion cell construction between anode and cathode sheets to prevent short-circuit and allow transfer of electrolyte ions through it. As such, it is an electrically insulating porous material and has the lowest thermal conductivity among all the material sheets in the internal stack of a Li-ion cell. The method of measurement was based on heat transfer through a semi-infinite medium for heat conduction. Thin heaters and temperature sensors were microfabricated on the surface of the separator sheet and the thermal response from the DC Joule heating was measured. This measured temperature response was compared with the theoretical temperature solution for a semi-infinite medium heat conduction model. The thermal conductivity was then determined when the experiment had been carried for sufficiently long time and steady state conditions were reached. Subsequently, from the transient temperature response, the specific heat capacity was calculated by using the previously measured thermal conductivity. The measured thermal conductivity for the separator was found to be $(0.5 \pm 0.03) \text{W m}^{-1} \text{K}$ and the specific heat capacity $(2480 \pm 300) \text{J kg}^{-1} \text{K}^{-1}$. However, their experiment was based on a Li-ion separator sheet only and not the whole Li-ion cell assembly. In order to use these values, the knowledge of the cell assembly is still required such as number of sheets, number of rolls and thickness of joint sections. Secondly, the separator sheet material and thickness used by manufacturers may be different than the one used in their work.

Bazinski & Wang [8] studied the influence of surface temperature and state of charge (SOC) on thermophysical properties of a Lithium Iron Phosphate (LFP) pouch cell. The state of charge is an estimate of the available energy capacity expressed as percentage of a reference capacity which usually is the rated capacity of a new cell (described more in Chapter 2). Their work was based on using an IHC which comprised of a battery sandwiched between aluminum platens acting as heat sinks. The heat generated by the battery was sensed by heat flow sensors which were placed between battery and aluminum platens. They concluded that the influence of SOC on specific heat capacity is very weak and can be neglected for cell modeling. However, the influence of temperature on specific heat capacity warrants consideration in modeling. Over full temperature range from $-5 \text{ }^\circ\text{C}$ to $55 \text{ }^\circ\text{C}$, this property can vary by 38%. In addition, the increase in current rate of charge/discharge will generate more heat which will change the temperature of the cell and consequently the specific heat capacity of the cell will change. The through-plane thermal conductivity was found to be independent of the temperature across its full SOC range. However, they did not study the in-plane thermal conductivity and heat generation from

the Li-ion cell. The values of through-plane thermal conductivity and specific heat capacity were measured for a Li-ion pouch cell only with a capacity of 14 A h. The capacity of the cell will govern the internal configuration and consequently affect its thermal properties.

Löwen, et.al. [9] worked with an isothermal calorimeter to measure the heat capacity of liquid and metal samples by using the dynamic correction constant of the calorimeter. The dynamic correction of isothermal calorimeters is based on the Tian correction equation (more details are discussed in Chapter 2). The equation corrects the output signal from heat flow sensors in time domain for a delay due to thermal mass of material between the source of heat and the heat flow sensor. The value of the dynamic correction factor signifies the thermal mass of the sample and can be used for measurement of specific heat capacity of samples. This method yielded results within an uncertainty of less than 4%. The calorimeter used for measurement had a sample holder cup which was an issue for samples with low conductivity, especially liquids as compared to metals (see Figure 2.6). The advantage of this method was its simplicity and quick experiment durations. The method, however, has never been applied for battery heat capacity measurement.

The literature work highlights that the lack of methods for measurement of all the thermal parameters and heat generation for different current-rates during charging and discharging, in order to complete the thermal characterization of Li-ion cells. Moreover, they show variation in thermal properties measured for similar Li-ion cells which further enforce the requirement of measurement for current Li-ion cells under consideration. The heat generation also varies as per the configuration of the cell by the manufacturer and thus has to be measured by using the isothermal heat conduction calorimeter in the lab.

1.3 Purpose

The purpose of this thesis work is to develop experimental methods using a custom-made IHC, which enable accurate measurement of the heat generation during charge and discharge for different current-rates and thermal characterization of Li-ion cells. The methods will be developed to measure thermal parameters such as specific heat capacity, through-plane thermal conductivity and in-plane thermal conductivity for Li-ion cells, by suitably modifying the custom-made IHC. These parameters can then be utilized in thermal modeling of Li-ion batteries.

1.4 Scope

The main focus has been to retrieve the thermal parameters and the heat generated during charging and discharging operation for different Li-ion cells. In order to do these experiments, a custom-made calorimeter was provided as well as access to other equipment and tools in the battery lab at Volvo GTT. The designed methods have been verified by testing samples of similar thermal properties as expected for Li-ion cells. The physical size and type of the calorimeter has limited the overall size to 122 mm × 215 mm, and form factor of the Li-ion cell to pouch and prismatic type for testing. The experiment environment in an ideal scenario should have been completely isolated from the surrounding, however the allocated experimental area was affected by lab temperature conditions. In addition, the effect of temperature on different properties of the Li-ion cells have not been studied and all the results are based on room temperature conditions of around 20 °C. The effect of state of charge and state of health (age effects) on the thermal parameters has not been considered in this thesis work as well.

Report structure

In chapter 2, theoretical background is provided on different types of Li-ion cells, calorimeter devices and their working principles as well as heat transfer equations which are utilized in the designing of the measurement methods. In chapter 3, the experimental setup is described in general which includes the general schematic of the IHC setup and measurement-recording devices used during all the experiments. In addition, the custom-built isothermal calorimeter at Volvo GTT is described with its components for better understanding. The heat flow and temperature sensors are described as well, including the calibration methodology and relative offset measurement between the different temperature sensors. In chapter 4, 5 and 6, the development of the experimental method for through-plane thermal conductivity, in-plane thermal conductivity and specific heat capacity respectively are described. The developed methods are verified by testing on sample materials and the results are discussed as well in these chapters. They are then applied on Li-ion cells, both prismatic and pouch type, for measurement of thermal parameters. Moreover, the heat generated from the cells for applied charge and discharge for different load cycles are reported. Finally, the measured parameters are used in a three-dimensional cell thermal model for investigating the cell internal temperature during operation. Chapter 8 includes the main derived conclusions and defines additional future work within this domain.

1.5 Environmental & ethical aspects

The development and progress within the battery industry introduces questions regarding both the environment and ethics. It is therefore important to treat these aspects in relation to this thesis work.

The rise of EVs and HEVs in the vehicle industry has become an important part of the automobile market [10]. The electric cars are often referred to as the zero emission vehicles which have been discussed worldwide for decades. However, as the technology improves both for the utilization and production the environmental gain is evident compared to ICEs [11]. Furthermore, as the key-component in the vehicles is the Li-ion batteries, the upcoming issues regarding the battery life-time have to be taken care of. To get a sustainable production and utilization of Li-ion batteries the life-time should be extended as far as possible and the recycling process has to be improved [10]. The incentives of recycling lithium has been very low until now since it has been a non-profitable market, but the growing interest in lithium might change this. In order to extend the life-time of the Li-ion batteries the operating conditions have to be optimized - which is where the thermal management is of high importance [5]. Not only would the safety increase if the temperature could be monitored and regulated, but also the life-time of the Li-ion cells. Thus, the batteries do not have to be replaced that often, which would result in better utilization of resources and less negative effects on the environment. Moreover, if the economical incentives and feasibilities grows even more, the EVs and HEVs would phase out the traditional ICEs. However, the Li-ion batteries will play a big role both locally as well as globally in the environmental challenges.

When conducting an experimental thesis work there are always ethical issues to consider. Here, the IEEE code of ethics are utilized as a reference. Regarding the first code of ethics in [12] the health, safety and welfare of the public could be affected by this study. If the results are utilized for thermal management systems in real life applications it could become both dangerous and costly if they are wrong. Thus, it is of high importance to establish good thermal parameters so that the thermal management system can be designed in a good way. The third code of ethics in [12] was of high concern in this thesis. The claims and results had to be presented in a honest way and with caution. Thermal experiments are always difficult to control which introduces ethical decisions whether the results are valid or not and if the measurement error are taken into account. If only the best results are chosen and presented this could give an inaccurate picture of how it really was. In addition, the collaboration between the people involved has made the second and eighth code of ethics in [12] important as well. The different culture background and also education have been a benefit rather than a source for unnecessary conflicts.

2

Technical background

This chapter provides a technical basis for better understanding of the work. First, an overview of lithium-ion battery cells is presented. Second, theory of the heat transfer used in the experimental design and modelling are provided. Last, the concepts of calorimetry are described.

2.1 Li-ion cells

There are numerous cell configurations available on the market today, with different forms and materials. The main function of a cell is to convert its contained chemical energy into electric energy through an electrochemical oxidation-reduction (redox) reaction [13]. A typical Li-ion cell consists of four major components as is shown in Figure 2.1.

1. The anode (negative electrode), which consists of an active material that is attached to a current collector.
2. The cathode (positive electrode), which also consists of an active material that is attached to a current collector.
3. The electrolyte, which is the ionic conductor that provides a path for the transfer of ions between the two electrodes. Some batteries use solid electrolytes but it is typically a liquid, such as organic solvents with salts to improve the ionic conductivity [13].
4. The separator, which is used to separate the electrodes mechanically and should block direct electron transfer between the electrodes while still maintaining a good path for the Li-ion transport [14].

In order to determine the standard potential of a cell, the oxidation potential of the anode and the reduction potential of the cathode are added together. The potentials for a couple of different cathode materials for Li-ion batteries can be seen in Figure 2.2 as where the potential of each chemistry is related to Li/Li^+ . It should be noted that the operational range of LMO (Lithium Manganese Oxide, $LiMn_2O_4$) and NMC (Lithium Nickel Cobalt Manganese Oxide, $LiNiCoMnO_2$) is limited to

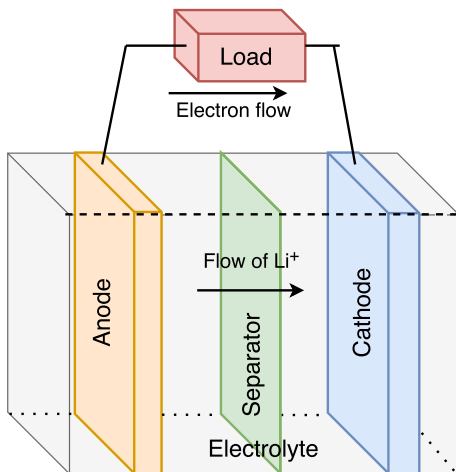


Figure 2.1: The electrochemical operation of a cell during discharge.

around 50 %. This is however not the case for LFP (Lithium iron Phosphate, $LiFePO_4$) and LTO (Lithium-titanate, $Li_4Ti_5O_{12}$) which can be utilized close to 100 % of their capacity. Regarding the anode material, graphite is widely used today due to cost and performance aspects but other materials such as LTO are also used. However, this results in a lower cell voltage which is evident from Figure 2.2.

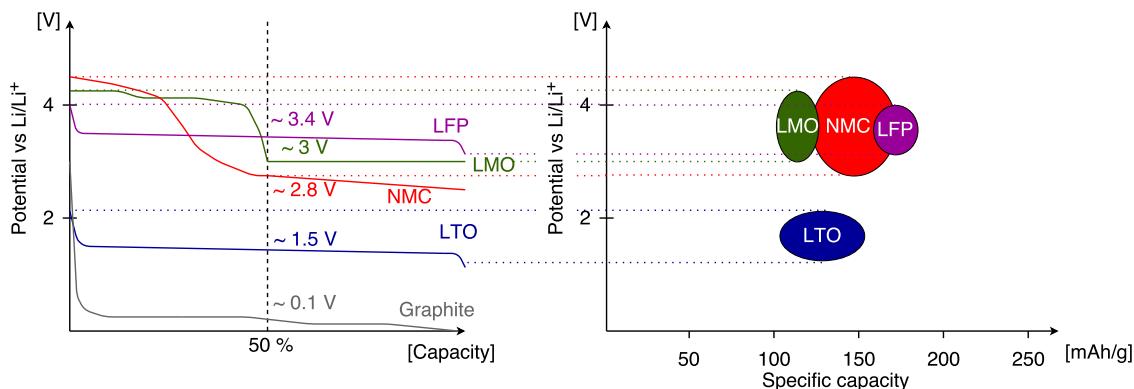


Figure 2.2: To the left the potential of a couple of different cathode materials is shown with reference to Lithium metal [3]. To the right the corresponding specific capacities for the materials are shown (retrieved from [15]).

Furthermore, the cells are optimized for either energy or power and will have different characteristics, which is difficult to combine in one cell [3]. Capacity of batteries are usually measured in Ampere-hours (Ah) and its energy in Watt-hours (Wh) [14]. This optimization is a trade-off that has to be chosen for a specific requirement or application. The current rate that is used will affect the cell performance greatly which can be seen in Figure 2.3 where the Ragone plot illustrates the available power and energy [3]. The property C-rate is the current normalized to cell capacity which means that 1C corresponds to charge/discharge in 1 h and 10C corresponds to 1/10 h [14]. By studying the Ragone plot it is evident that energy optimized cells (in area E) can only be used for low C-rates and power optimized cells (area P) suffer in energy content instead. Since the cell optimization is limited to the black line

the point Opt is an unreachable state. Therefore, many cells is found to be in the combined area E/P [3].

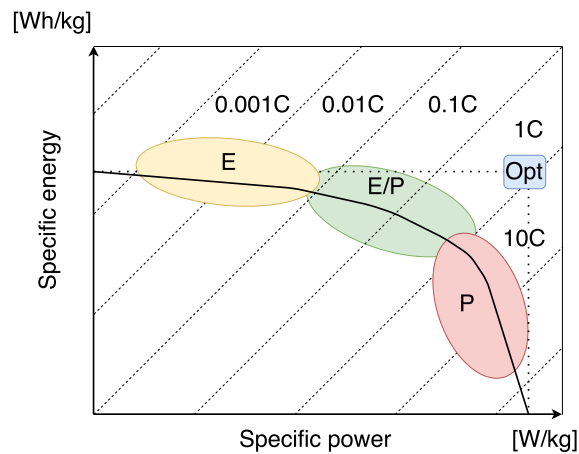


Figure 2.3: Ragone plot for cell optimization of energy (E-area) and power (P-area). Opt indicates the optimal, but unachievable, state whilst the E/P-area is a compromise of energy and power.

2.1.1 Cell designs

The three dominating Li-ion battery configurations used for EVs are prismatic, cylindrical and pouch cells [3]. Their appearance as well as important components for each design is shown in Figure 2.4.

Prismatic cell

Prismatic cells are typically metal enclosed stacks of alternated electrode layers with a separator in between as can be seen in Figure 2.4a with capacities typically in the range of 1-100 A h. The metal enclosure increase the stability of the cell but also the weight [16]. The scalability of the cell makes it suitable for both consumer electronics as well as EV-applications but there are many standard formats and the final design is dependent on the manufacturer. As the cells can swell due to malfunction or mistreatment, many prismatic cells are provided with a pressure vent port to prevent high pressure buildup which can also be seen in Figure 2.4a.

Cylindrical cell

Cylindrical cells are usually made out of long strips of electrodes that are wound into a cylindrical shape as can be seen in Figure 2.4b. The capacity of cylindrical cells are typically in the range of 0.5 - 50 A h. In addition, they are encapsulated in hard cases and often sealed with gaskets which improves the mechanical stability. The wound structure prevents the electrodes from separating during pressure buildup which makes the swelling less appreciable. Some cells are also provided with pressure vents. Cylindrical cell types are used in many different applications due to their fast

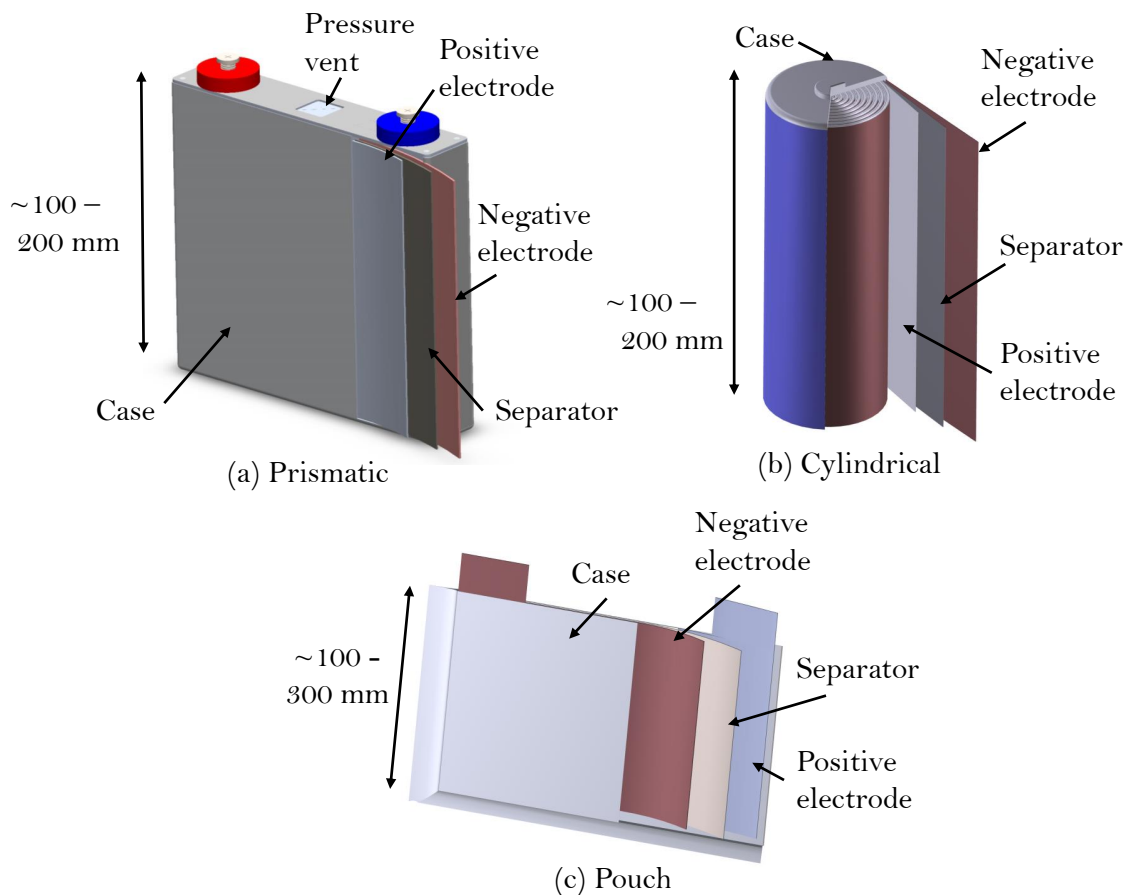


Figure 2.4: The three dominating li-ion cell types with their structure and composition.

assembly and low manufacturing cost including both consumer electronics as well as in HEVs and EVs [16].

Pouch cell

Unlike prismatic and cylindrical cells that are usually enclosed in a metal cover, the pouch cells are enclosed in foil pouches with heat-sealed seams as in Figure 2.4c. This makes them lightweight but the mechanical stability is poor [16]. The thin cells introduces the benefit of great stacking possibilities i.e. more efficient space usage but the risk of swelling cells is imminent and reduces the use in commercialized products. Thus, since it is not having its own mechanical stability, the surrounding material has to provide this. Moreover, different cell performance characteristics can be achieved by the placement of the terminals [3]. A power-optimized cell often has its terminals on opposite sides of the cell whilst energy-optimized cells usually have their terminals on the same side as in Figure 2.4c. The capacity of pouch cells are usually in the range of 0.1 - 100 A h.

2.1.2 Equivalent circuit battery model

In order to understand the working principles and function of Li-ion batteries there are some parameters that are important to study. A simple model of a battery can be seen in Figure 2.5 as where the OCV (open circuit voltage) is dependent on the SOC (state of charge) [17]. The OCV is the voltage of the cell under no-load conditions and is usually close to the theoretical cell voltage [13]. The SOC can in turn be explained as the charge state of the battery ranging from 0-100%. Moreover, the internal resistance (R_{int}) is the sum of several resistances within the cell, e.g. resistance in the active electrode materials, ionic resistance in the electrolyte and interface resistances between the different interfaces inside the battery [3]. This internal sum of resistances is also dependent on the SOC and gives rise to so called Ohmic losses. The R_{int} causes a voltage drop (IR drop) which is directly proportional to the current through the battery. The terminal voltage (V_T) of the battery will therefore be $V_T = OCV(SOC) + I \cdot R_{int}(SOC)$.

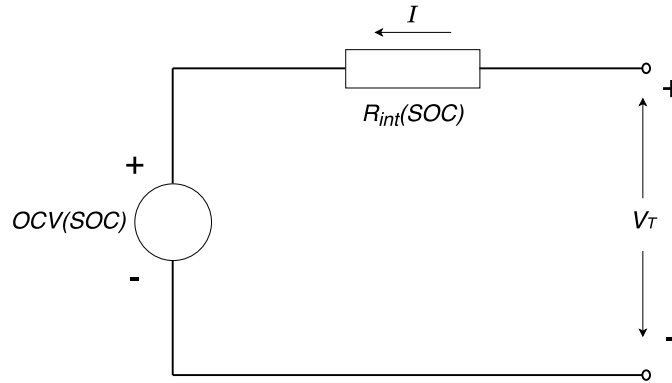


Figure 2.5: Simple battery model with internal resistance.

2.2 Heat transfer

Three dimensional heat diffusion equation in cartesian coordinates [18] can be defined as

$$\frac{\partial}{\partial x} \left(k \frac{\partial T}{\partial x} \right) + \frac{\partial}{\partial y} \left(k \frac{\partial T}{\partial y} \right) + \frac{\partial}{\partial z} \left(k \frac{\partial T}{\partial z} \right) + q = \rho c_p \frac{\partial T}{\partial t} \quad (2.1)$$

where, $k = k(x, y, z)$ is thermal conductivity [$\text{W m}^{-1} \text{K}^{-1}$] dependent on spatial coordinates x, y & z , T is temperature at a particular (x, y, z) location within the body, ρ is the mass density, c_p is the specific heat capacity [$\text{J kg}^{-1} \text{K}^{-1}$], t is the time and q is the heat generation per unit volume. This equation, often referred to as the heat equation, provides the basic tool for heat conduction analysis. From its solution, the temperature distribution $T(x, y, z)$ can be obtained as a function of time. The apparent complexity of this expression should not obscure the fact that it describes an important physical condition, that is, conservation of energy.

For example, the term $\frac{\partial}{\partial x} \left(k \frac{\partial T}{\partial x} \right)$ is related to the net conduction heat flux into the control volume for the x-coordinate direction. That is, multiplying by dx gives

$$\frac{\partial}{\partial x} \left(k \frac{\partial T}{\partial x} \right) dx = q_x'' - q_{x+dx}'' \quad (2.2)$$

with similar expressions applying for the fluxes in y - and z -directions. Equation (2.1) can be further modified for anisotropic material with properties categorised as per direction.

$$k_x \left(\frac{\partial^2 T}{\partial x^2} \right) + k_y \left(\frac{\partial^2 T}{\partial y^2} \right) + k_z \left(\frac{\partial^2 T}{\partial z^2} \right) + q = \rho c_p \frac{\partial T}{\partial t} \quad (2.3)$$

For steady state heat transfer and no internal volumetric heat generation, (2.1) now takes the form

$$\frac{\partial}{\partial x} \left(k \frac{\partial T}{\partial x} \right) + \frac{\partial}{\partial y} \left(k \frac{\partial T}{\partial y} \right) + \frac{\partial}{\partial z} \left(k \frac{\partial T}{\partial z} \right) = 0 \quad (2.4)$$

This model can be used for measurement of thermal conductivity during steady state experiments. The experiment design has to ensure that the path of heat flow is unidirectional so as to neglect other components in other directions.

The heat generation within the cell can be expressed as in [4]

$$Q_t = I(V - V_{OCV}) + IT_c \frac{dV_{OCV}}{dT_c} \quad (2.5)$$

where I is the charge or discharge current (positive for charge and negative for discharge), V_{OCV} is the open circuit voltage, V is the cell voltage, $\frac{dV_{OCV}}{dT_c}$ is the entropy coefficient. The first term on the right is the heat generated by cell overpotential which is irreversible and always positive, whereas the second term is the reversible entropic heat, which can be either positive or negative dependent on the direction of current and also the sign of the entropy coefficient.

2.3 Calorimeters and calorimetry

A calorimeter is a device used for measurement of heat. In all calorimeters the calorimeter vessel (alternatively denoted by some authors as cell, container or calorimeter proper) is in very good contact with the sample. Moreover, the surrounding is often called a shield, environment or thermostat. Some calorimeters can have several shields to further isolate the calorimeter.

In calorimeters which do not undergo mass exchange with the surrounding, the heat power equation has been described by Zielenkiewicz & Margas [19] as

$$P(t) = G(T_c(t) - T_0(t)) + C \frac{dT_c(t)}{dt} \quad (2.6)$$

where $P(t)$ is heat power, G is heat transfer factor based on Newton's cooling law, $T_c(t)$ is time varying temperature of calorimeter vessel and $T_0(t)$ is time varying temperature of calorimeter shield or surrounding, ΔT is temperature difference between calorimeter vessel and surrounding.

On the basis of (2.6), the calorimeters have been divided into two major groups:

- I. Adiabatic calorimeters in which the temperature gradient between the calorimeter shield and vessel is zero ($\Delta T = 0$).
- II. Non-adiabatic calorimeters in which the temperature gradient between calorimeter shield and vessel is not zero ($\Delta T \neq 0$).

Two subgroups of adiabatic calorimeters can be distinguished:

- i. Calorimeter with constant shield temperature $T_0(t)$. They can be called adiabatic-isothermal.
- ii. Calorimeter where temperature of the shield $T_0(t)$ changes with time. They can be called as adiabatic-nonisothermal or simply adiabatic.

In addition, nonadiabatic calorimeters have two subgroups:

- i. Calorimeter with constant shield temperature $T_0(t)$ called isoperibol calorimeter.
- ii. Calorimeter where temperature of the shield $T_0(t)$ changes with time. An example of this type of calorimeter is scanning calorimeters.

The isoperibol calorimeter have a temperature gradient which is stable in time. They can also be denoted as non-adiabatic isothermal calorimeters [19]. The custom-made calorimeter in the battery lab at Volvo GTT can be classified in this category of non-adiabatic isothermal calorimeters.

2.3.1 Isothermal heat-conduction calorimeter

Isothermal operation of a calorimeter is normally defined as where the calorimeter shield has a constant temperature [20]. A general construction of heat conduction is shown in Figure 2.6. The sample in the cup (cup used only for liquids) is placed between two heat flow sensors (called thermopiles). The thermopiles are in direct contact with heat sinks maintained at a constant temperature. The heat sinks are usually made from aluminum and has an internal channel for coolant circulation.

In heat conduction calorimetry, the heat flow sensors are of high importance since they are measuring the thermal power, $P = dQ/dt$, generated within the sample. However, the instantaneous power is generated from measured power by applying a Tian correction equation [21] (explained more in 2.3.3). The integration of the thermal power output from thermopiles gives the total heat Q . When heat is gen-

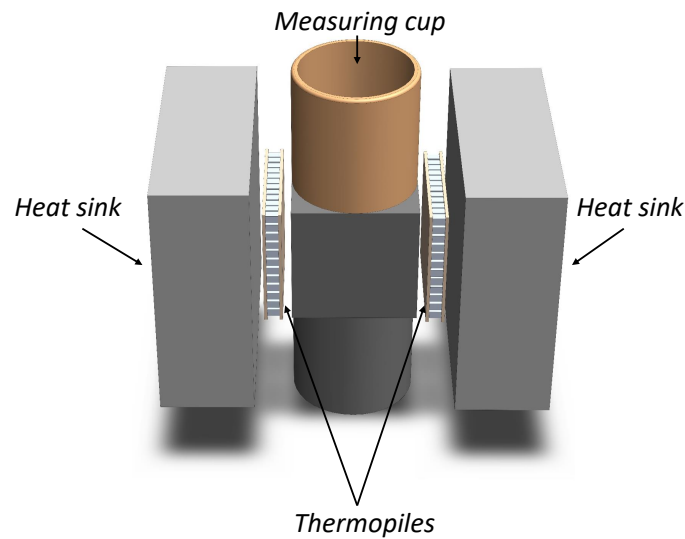


Figure 2.6: Principle CAD of an isothermal conduction calorimeter

erated or absorbed in the sample, its temperature rises or falls respectively relative to stable heat sink temperature conditions. The resulting temperature difference between sample and the heat sink gives rise to a heat flow through the heat flow sensors that can be measured. Note that the heat-flow sensors generate a voltage that has to be converted into the thermal power, i.e. the power is not measured directly.

2.3.2 Calibration of IHC

The conversion of thermopile voltage output to measured thermal power is done by a multiplication coefficient called the calibration factor ε . It is evaluated by calibrating the output of thermopiles against a known input thermal power.

In order to calibrate an IHC either of the two proposed methods, steady-state and pulse, described in [21] can be used. The two alternatives are shown in Figure 2.7 as where a known heat is released inside the calorimeter (represented by red curve) whilst the thermopile voltage signal is measured (represented by blue curve). Note that the voltage signal (blue curve) initially lags the input power (red curve) due to thermal inertia of calorimeter (described more in section 2.3.3). The baseline in the curve is the output from the thermopiles under steady conditions when no heat is being generated in the calorimeter cell. These baselines shifts to higher or lower levels based on the change in the surrounding temperature of the calorimeter as well as the surrounding. The voltage output from the thermopiles has to be corrected for this baseline value in order to measure the contribution from the heat generated in the sample only.

The calibration factor ε can then be calculated as

$$\varepsilon = \frac{P}{U} \quad (2.7)$$

for steady-state, where U is the baseline corrected sensor voltage and P the input power. If pulsed calibration are to be used instead the calibration factor is calculated as

$$\varepsilon = \frac{P \cdot \Delta t}{\int U dt} \quad (2.8)$$

where U is the baseline corrected sensor voltage, Δt the power pulse duration and P the input power.

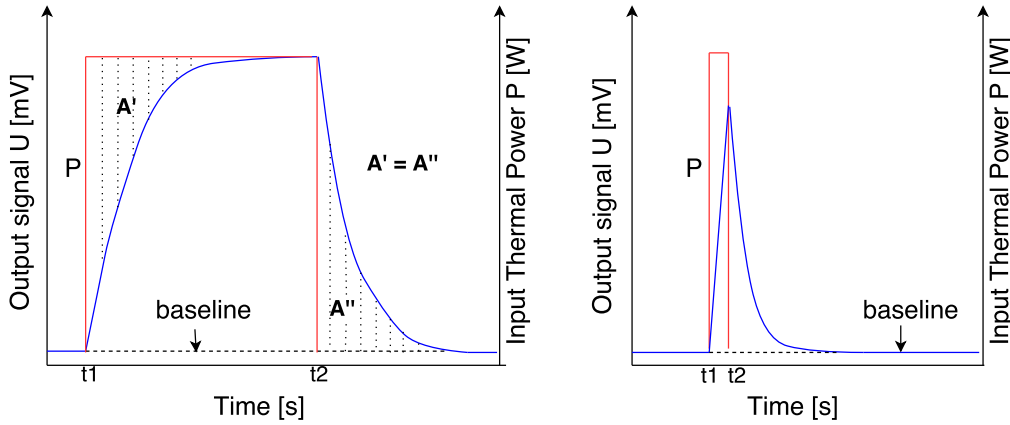


Figure 2.7: Steady state calibration (to the left) where a constant thermal power is used. Pulse calibration (to the right) where a pulsed power is utilized. The baseline has to be subtracted for both methods.

2.3.3 Thermal output and dynamic correction

The general heat power equation of calorimeters represented previously by equation (2.6) can be modified for isothermal calorimeters since shield temperature T_0 is constant and independent of time. The difference between calorimeter vessel temperature $T_c(t)$ and shield T_0 can be represented by a single function $T(t)$. Thus, the equation changes to

$$C \frac{dT(t)}{dt} + GT(t) = P(t) \quad (2.9)$$

or in the form

$$CdT(t) + GT(t)dt = P(t)dt \quad (2.10)$$

Here it is assumed that the general calorimeter has a temperature sensor as measuring output in $T(t)$ values. If however, the output from the IHC is measured in

2. Technical background

a different physical quantity β such that $\beta = T \cdot g$ where g is the proportionality constant, then equation (2.9) is modified to

$$\frac{C}{g} \cdot \frac{d\beta(t)}{dt} + \frac{G}{g}\beta(t) = P(t) \quad (2.11)$$

This can be solved to get values of thermal power in time expressed as a function of measured output β . Equation (2.11) is referred to as Tian-Calvet equation [19]. The Tian constant τ can be denoted as ratio of heat capacity C to heat transfer factor G and then (2.11) can be modified to

$$\tau \frac{d\beta(t)}{dt} + \beta(t) = P(t) \frac{g}{G} = f(t) \quad (2.12)$$

For steady state conditions, the temperature gradient becomes constant and the output of calorimeter is denoted as β_t . We can then apply this constant to derive a solution for equation (2.12) as

$$\beta(t) = \beta_t(1 - e^{-\frac{t}{\tau}}) \quad (2.13)$$

which is the general solution for the output of a isothermal calorimeter.

In order to evaluate the calorimetric results from the provided IHC, there are essentially three different properties that should be considered: the baseline U_0 (V), the calibration coefficient ε (W V⁻¹) and the time constant τ (s) [21]. The baseline and the calibration coefficient are used to calculate the steady state power from the calorimeter, i.e. to convert the measured voltage into the steady thermal power as

$$P(t) = \varepsilon(U(t) - U_0(t)) \quad (2.14)$$

The Tian constant τ is coupled to the thermal parameters of the calorimeter materials and design. It can either be approximated by the steady state fall time (to 36.8 % of initial steady state value from equation (2.13)) or by theoretical calculations (ration of C and G).

If the output of the provided IHC is in voltage U from thermopiles, the Tian-Calvet equation (2.11) can be represented by

$$P_c(t) = \varepsilon \left(U(t) + \tau \frac{dU(t)}{dt} \right) \quad (2.15)$$

where P_c denotes the corrected power for the transient in consideration. This correction can be applied to the raw output signal as shown in figure 2.8 to correct for the thermal power.

If the assumption that the calorimetric vessel and the investigated sample are at the same temperature is not valid, an additional coefficient has to be added. If the power balance equation for the sample and the power balance equation for the

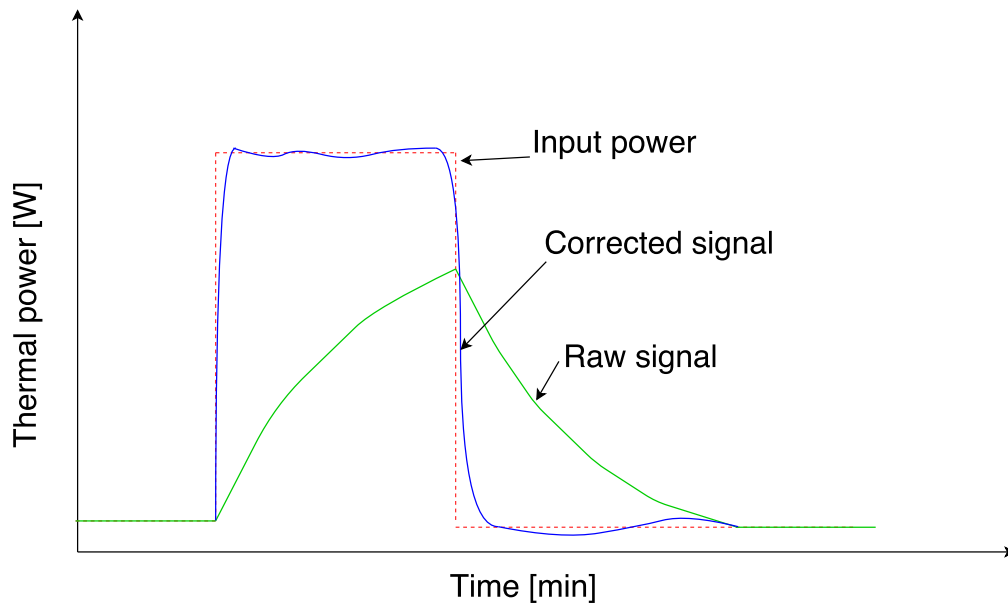


Figure 2.8: Application of Tian equation to raw signal from a calorimeter

calorimetric cell are combined (see [22] for theoretical details) this results in the formulation

$$P_c = \varepsilon \left[U(t) + (\tau_1 + \tau_2) \cdot \frac{\partial U(t)}{\partial t} + (\tau_1 \cdot \tau_2) \cdot \frac{\partial^2 U(t)}{\partial t^2} \right] \quad (2.16)$$

where the Tian constant is now divided into τ_1 and τ_2 . Thus, the thermal inertia of the system can be described by τ_1 which is coupled to heat capacity and heat exchange parameters whilst τ_2 is related to the internal temperature gradients [22].

2. Technical background

3

Experimental setup

This chapter describes the experimental setup of the thesis work. It outlines the general schematic of IHC connection to sensors, recording equipment and computer. The construction and calibration of the IHC are also presented here.

3.1 General setup

Volvo GTT had previously acquired a custom-made isothermal conduction calorimeter for carrying out measurements of heat generation. The working principle for this type of calorimeter was explained in section 2.3. The acquired calorimeter had to be setup before measurements could be carried out.

The general setup for the experiments is as shown in Figure 3.1. A calorimeter with two sides, labeled A and B, was used to sandwich the sample at the center which reduces the heat loss from the sample.

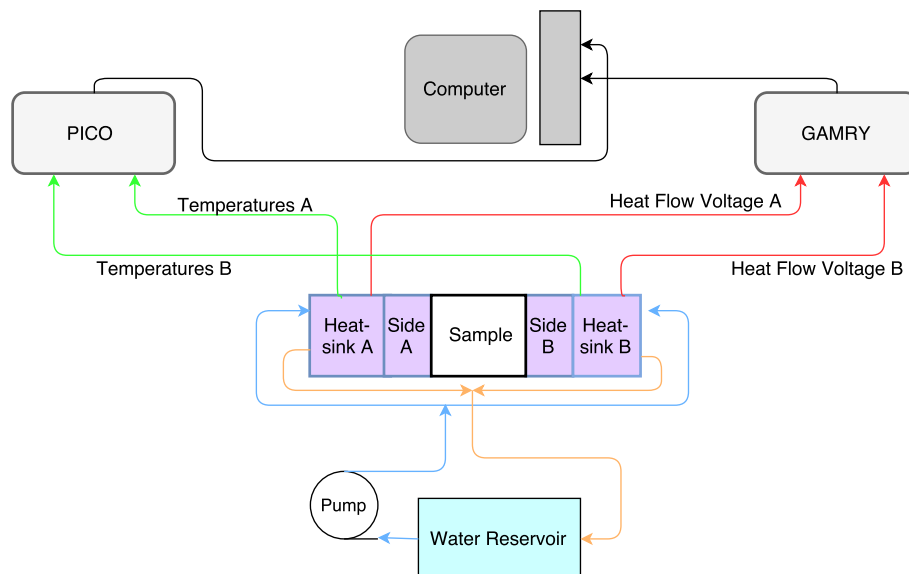


Figure 3.1: Schematic of experimental setup showing measuring devices and calorimeter layout

3. Experimental setup

The CAD schematics for the calorimeter can be seen in Figure 3.2. There are 6 heat flow sensors [23] mounted on each calorimeter side making it a total of 12 for both calorimeter side A and B. The heat sink for both side A and B is made from two aluminum plates which have a water flow channel machined into them. The channel is sealed when both plates are assembled together, by an O-ring fitted around it. Moreover, the pressure plates have tension spring holders used to keep the Li-ion cell in good contact with the calorimeter.

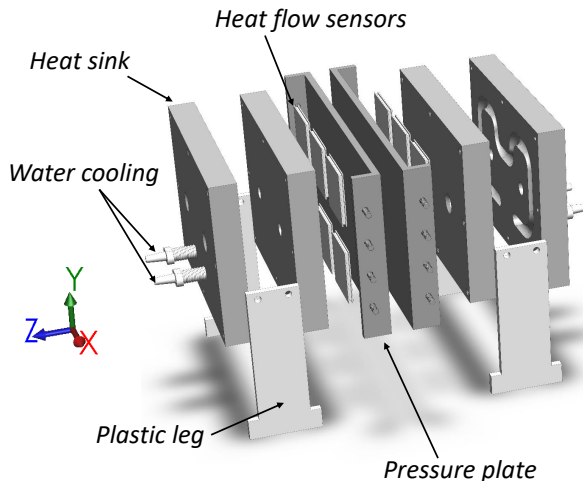


Figure 3.2: CAD of the calorimeter assembly made in Solidworks.

The voltage output from both side heat flow sensors are combined to get the final output of the setup. Voltages are recorded using a GAMRY electrometer [24], which is presented in section 3.2 along with the other measurement setup. Temperature sensors of PT100 type were used to sense the change in temperature at different locations of the calorimeter side A and B. PICO-104 recorders were utilized to record the data from the PT100 sensors which enabled 8 channels for temperature measurements in total. In addition, the heat-sinks of the calorimeter were kept at isothermal temperatures using a large water reservoir and a pump arrangement. Finally, the calorimeter was surrounded by glass wool insulation to reduce heat losses to the surrounding.

In the later stages of thesis work, the water reservoir and pump arrangement was replaced by an isothermal bath system JULABO F25MA, which can regulate temperature around $\pm 0.02^\circ\text{C}$ [25]. This modification was made as per availability of equipment.

3.2 Measurement equipment

The measurement equipment used for monitoring and feeding voltage and current to the setup was the GAMRY Reference 3000 potentiostat with an auxiliary electrometer. This instrument utilizes four terminal measurement in order to get high

resolution and accuracy of the measurements. The operating mode used for all the measurements was the PWR 3000 which offers the opportunity to read voltage for selected channels as well as charging with a custom current level. Also, it offers two different compliance voltage and current settings. Either a higher voltage range of ± 30 V for a compliance current of ± 1.5 A or a lower voltage range of ± 15 V for a compliance current of ± 3.0 A. In addition, the eight auxiliary channels that are included for this instrument can measure a ± 5 V signal superimposed on a common mode voltage up to ± 36 V [24]. The used specifications as well as the measurement uncertainties for this GAMRY instrument can be found in Table 3.1.

For the temperature measurement, platinum resistance thermometers of type PT100 class B 1/3 DIN were used. The principle is that the resistance of the PT100 element is measured (which should be $100\ \Omega$ at $0\ ^\circ\text{C}$) and can be linearized within the range of 0 to $100\ ^\circ\text{C}$ according to the International Temperature Standard 90 (ITS-90). For the PT100 sensor a $1\ ^\circ\text{C}$ will cause a resistance change of $0.384\ \Omega$ [26]. Therefore, the chosen method was to use 4-wire measurement in order to eliminate the effect of the feeding wires. To record and convert the resistance readings from the PT100 sensors the PT-104 temperature data logger [27] instrument with its PICO software was used. The specifications such as the compatibility and accuracy can be found in Table 3.1.

Table 3.1: Measurement equipment used in the experimental setup as well as the measurement accuracies for the different instruments.

GAMRY 3000 Reference	
Operation limits	± 15 V; 3.0 A or ± 30 V; 1.5 A
Potential applied accuracy	± 1 mV $\pm 0.2\%$ of setting
Potential measured accuracy	± 1 mV $\pm 0.2\%$ of reading
Current applied/measured accuracy	± 5 pA $\pm 0.05\%$ of range $\pm 0.2\%$ of value (3 A - 3 nA)
PT-104 Data Logger	
Compatibility	Works with PT100 and PT1000 sensors
Accuracy (unit at $23 \pm 2\ ^\circ\text{C}$)	$0.015\ ^\circ\text{C}$ $+0.01\%$ of reading
Resolution	$0.001\ ^\circ\text{C}$
FLUKE 787	
Accuracy ($40\ \text{k}\Omega$ range)	0.2% of reading + 1 count (resolution of $0.01\ \text{k}\Omega$)
Accuracy ($400\ \text{k}\Omega$ range)	0.2% of reading + 1 count (resolution of $0.1\ \text{k}\Omega$)
VERNIER Mitutoyo Digital	
Accuracy (length $< 200\ \text{mm}$)	$\pm 0.02\ \text{mm}$

For the resistance measurements that had to be conducted, a FLUKE 787 instrument was used. In order to limit the current going through the voltage dividers a higher resistance was desirable. Thus, the accuracy for the two ranges considered is shown in Table 3.1.

The last important measurement equipment was the heat flow sensors. The setup

has 6 thermopile modules on each calorimeter side which utilizes the Seebeck effect to generate a voltage. The Seebeck effect is the direct conversion from heat to electricity at the junction of different wire types. They are attached with their "cold" side onto the heat-sink in a (2x3) matrix as seen in Figure 3.2 and are coupled in series to measure the total generated voltage.

3.3 Calibration

The heat flow sensors are used to measure the heat flow in watts while the output of the sensors is in units of volt. Therefore, it was needed to calibrate the setup and experimentally evaluate the calibration coefficient. To calibrate the setup, i.e. to find the conversion factor ε as explained in section 2.3.1, a known input of heat had to be measured along with the recorded voltage. In addition to the existing setup a calibration heater was built and adapted to the measurement equipment. Also, a temperature sensor performance test was conducted.

3.3.1 Calorimeter setup

For the calibration of the calorimeter, i.e. the retrieval of the calibration coefficient ε (see section 2.3.2), the manufactured calibration heater was sandwiched between the two calorimeter sides as in Figure 3.3. The temperatures were monitored using the PT100 sensors at particular locations inside the different calorimeter parts. The locations were inside the heat sinks, the pressure plates and inside the calibration heater. Hereinafter those sensors will be referred to as Side A/B heat sink, Side A/B and Cell center. To insulate the setup it was surrounded by glass wool insulation.

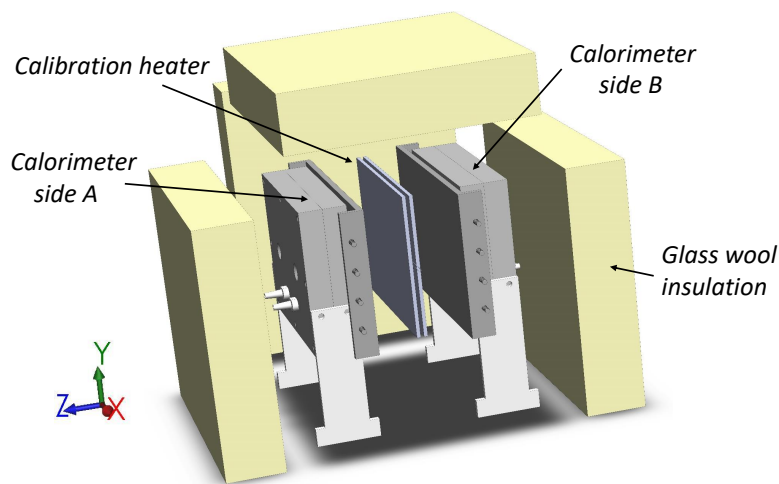


Figure 3.3: Setup for the calibration of the calorimeter with the bidirectional calibration heater sandwiched between the two sides.

3.3.2 Calibration heater

In order to both achieve good control of the power dissipated in the calorimeter, as well as a sample with known properties, a calibration heater was constructed. It was designed to have similar dimensions as the sample pouch cell (150x100x7 mm) which resulted in the dimensions 170x120x10 mm. In order to produce heat inside the calibration heater two silicon rubber heater mats [28], each with rated power of 15 W, was used. To isolate the two heater mats an isolation foam [29] was used and were finally encapsulated as a sandwich by two 3 mm thick aluminum plates to enable good contact. The calibration heater can be seen in Figure 3.4 with its electrical connections.

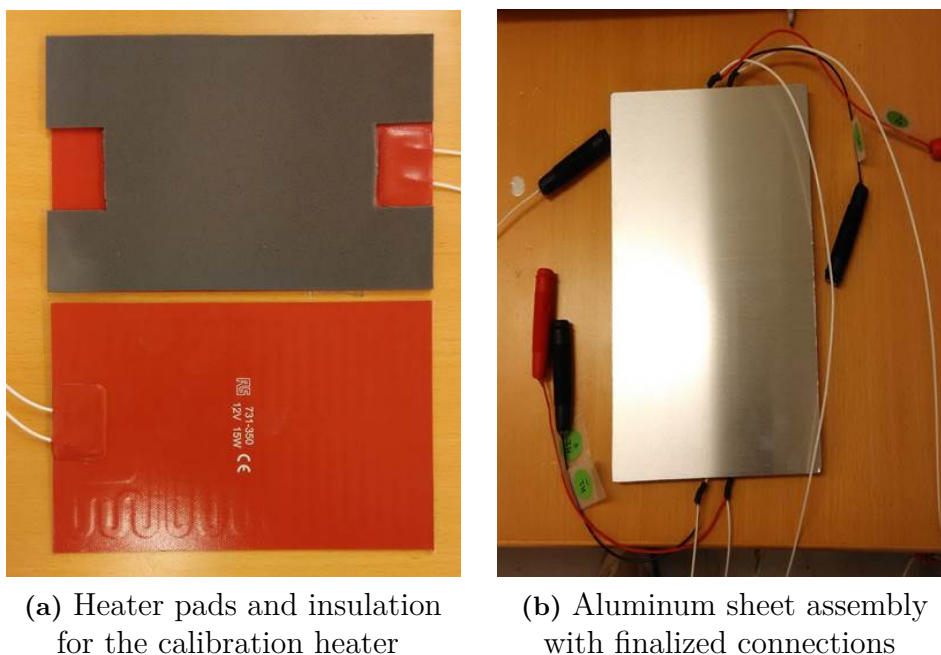


Figure 3.4: The inside and outside of the calibration heater with its heater pads, insulation and connections.

In order to measure the power produced in the heater mats as accurate as possible, the actual voltage applied to the heater mat terminals had to be measured. This was done by soldering the sensing cables onto the feeding cables close to the heater mat terminals. Since the rated voltage is 12 V for each heater mat and that the GAMRY auxiliary channels can only measure a voltage difference of ± 5 V, voltage dividers were needed. These voltage divider circuits were constructed so that the whole range of 12 V could be mapped onto 0-5 V. The chosen resistors in the series connection had the values 24 k Ω and 51 k Ω respectively as where the sensing cables from the GAMRY was probing the difference over the smaller of the two. This resulted in a maximum voltage of 3.84 V according to

$$V_{aux} = V_{act} \frac{R_1}{R_1 + R_2} = 12 [V] \frac{24 [k\Omega]}{51 [k\Omega] + 24 [k\Omega]} = 3.84 [V] \quad (3.1)$$

3. Experimental setup

where V_{aux} is the voltage input to the GAMRY auxiliary channels, V_{act} is the actual voltage applied on the heater mat, R_1 is the resistor which is measured across and R_2 is the high value resistor.

3.3.3 Calibration constant

The calibration was performed at three different power levels: 0.184 W, 1.65 W and 4.59 W. This was done to investigate the variation of calibration constant with input power. Moreover, if higher power levels would have been used that would start to heat up the thermal bath used for the calibration. The second run at 1.65 W is shown in Figure 3.5 to visualize how the system behaves during a measurement. It can be seen that the heat flow sensor voltages on calorimeter side A and side B are overlapping and have a maximum deviation of 0.6 % from each other. In addition, it is evident that the temperatures of the heat sinks do not increase significantly during the pulse and consequently returns to their initial value at the end of pulse. The final calibration results of the setup can be seen in Table 3.2 where the three specified power levels were used. It can be seen that the values of ε are not dependent on the power level and are not deviating much. Also, the average values for the two different sides are very similar which makes the total average value more trustworthy. In addition, the measurement uncertainty was calculated to 2.4 % and the derivation can be found in Appendix A.1.

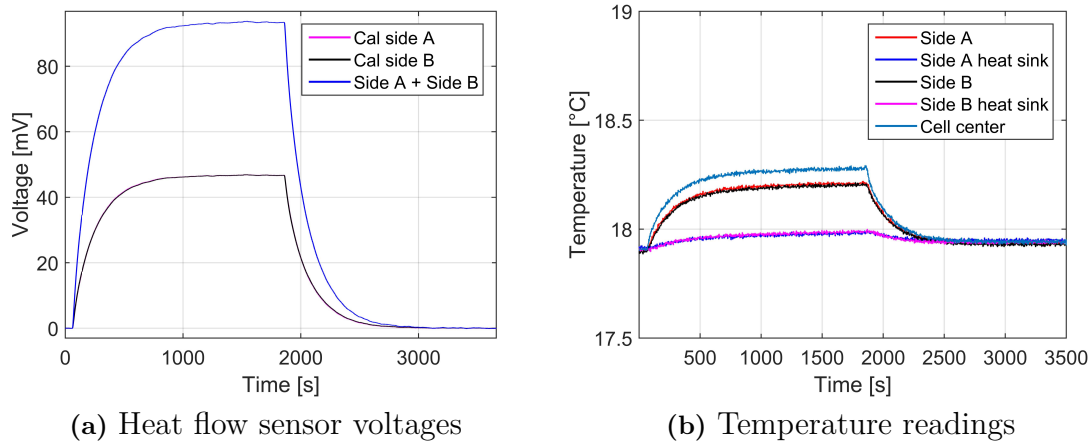


Figure 3.5: The heat flow sensor voltages as well as the temperature readings for the calibration with 1.65 W. Note that some signals are overlapping.

Even if the results were consistent the insulation of the setup could be improved. The glass wool is keeping most of the heat inside but there is still some heat loss to the surrounding.

Table 3.2: Measurement values from the steady-state calibration tests. The independent values for both the A-side and the B-side as well as the sides combined is shown with their average values and standard deviation.

Power	ε [W V^{-1}]		
	A-side	B-side	Total
0.184 W	17.585	17.760	17.672
0.184 W	17.559	17.556	17.558
1.65 W	17.466	17.492	17.479
1.65 W	17.653	17.692	17.672
4.59 W	17.610	17.655	17.633
4.59 W	17.756	17.492	17.622
Avg	17.6048	17.6078	17.6060
σ	0.097	0.110	0.076

3.3.4 Validation of calibration constant

In order to validate if the calibration factor was working properly it was necessary to estimate the power from a known input. This means that the power was to be back-calculated from the heat flow voltage measurements. As the actual input power was known the comparison between the back-calculated power (using $\varepsilon = 17.606 \text{ W V}^{-1}$) and the actual power is shown in Figure 3.6. The maximum deviation from the actual input power during steady state was $\approx 0.6\%$ and the two baselines before and after are close to the same values. In addition, the sensitivity is highlighted in Figure 3.6 to show that the calorimeter is able to measure power levels down to $\approx 10 \text{ mW}$.

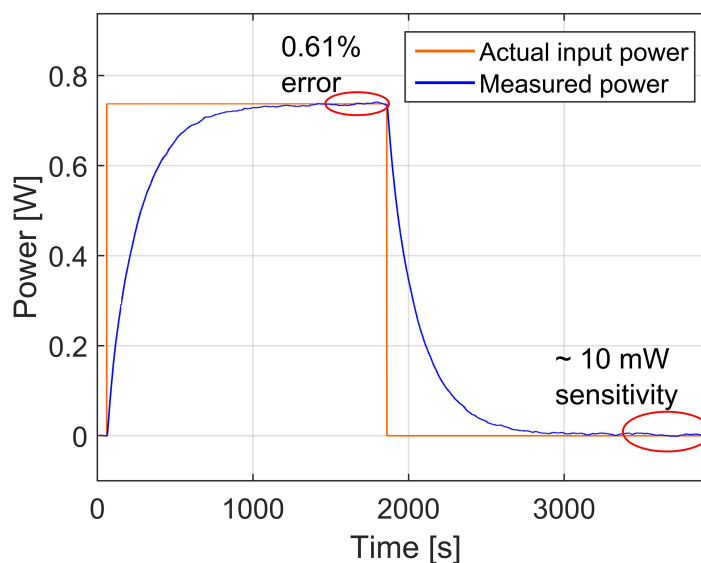


Figure 3.6: Measurement of the output power based on calibration constant.

3.4 Temperature sensors

Measurement of the thermal parameters for different cells is dependent on the differential temperature readings of the PT100 sensors and not the absolute temperatures. Therefore, a performance study of the PT100 sensors had to be conducted. A copper plate with stainless steel clamps was utilized. The setup can be seen in Figure 3.7 as where the copper plate was then submerged in water while the PT100 sensors were kept just above the water level ensuring dry working conditions.

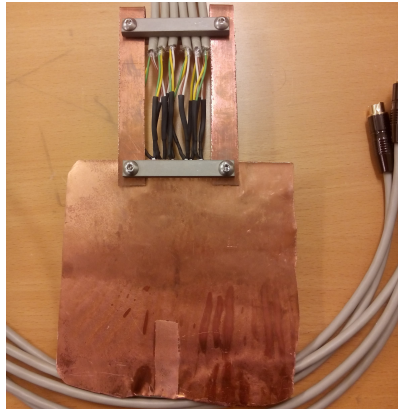
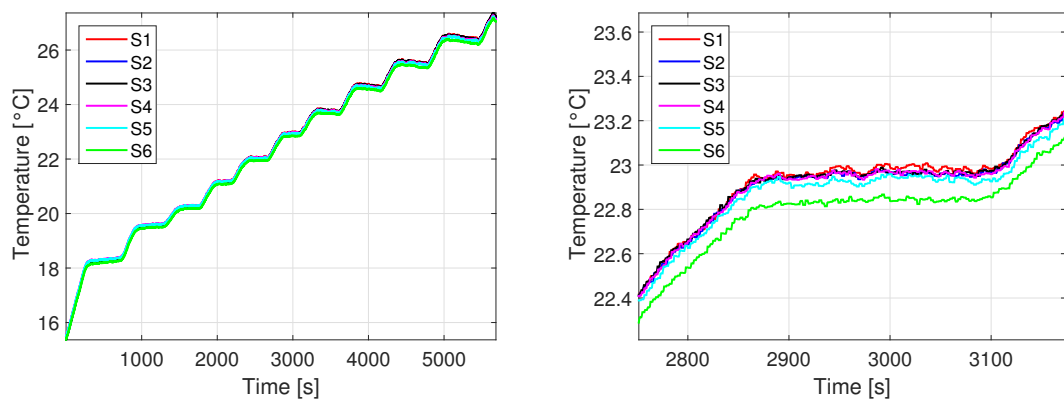


Figure 3.7: PT100 comparison setup where the copper plate was submerged in water whilst the sensors were kept in the air.

The high thermal conductivity of the copper plate ensured that the sensors were subjected to the same temperature. The outcome of this study was to evaluate the offset and the gain when comparing the PT100 sensors at different temperature levels. The temperature levels were maintained by utilizing a Lauda E100 immersion circulation thermostat [30]. The result of the study can be seen in Figure 3.8 for different temperature levels.



(a) Temperatures for the 6 PT100 sensors over the range of 18-27°C

(b) Zoomed in temperature sensor data to see the offset levels

Figure 3.8: Temperature sensor calibration for different temperature levels.

In Figure 3.8b it can be observed that there is an offset for the S6 sensor whilst the other sensors lies within $0.1\text{ }^{\circ}\text{C}$. In addition, there is gain for each individual sensor which makes them diverge for rising temperature. It can be noted as well that the Lauda E100 thermostat is not able to keep the water bath at a particular temperature as the overall temperature of the bath is increased.

The study was helpful in selection of PT100 sensors with similar performance characteristics (showing negligible offset or gain) for measurement of differential temperature in thermal properties measurements.

4

Measurement of through-plane thermal conductivity

This chapter describes the method development for the measurement of through-plane thermal conductivity. The method was validated by carrying out measurements on sample materials. The results of the measurements are presented at the end of the chapter.

4.1 Method development

The thermal conductivity of a prismatic or pouch type cell can be categorized into three components: through-plane (z-direction), in-plane horizontal (x-direction) and in-plane vertical (y-direction).

The initial experiment setup was designed from the general setup by modifying it as shown in Figure 4.1. The calorimeter side B was removed and the setup was insulated from the environment on that side to force heat along the z-direction towards the heat sink A. This reduced the experiment time as well. This uni-directional heat flow was aided by insulating the whole setup, thereby restricting the heat flow in x- and y-direction. The one dimensional steady state heat conduction equation can be derived from the general three dimensional heat conduction equation (2.4) by assuming constant heat flux boundary condition as

$$\frac{q}{A_{xy}} = -k_z \frac{\partial T}{\partial z} \quad (4.1)$$

where, k_z = through plane thermal conductivity ($\text{W m}^{-1} \text{K}^{-1}$), q = heat flux (W), A_{xy} = cross section area (m^2), z = through plane thickness of sample (m).

The temperature drop across the thickness of the sample was to be measured with PT100 sensors which have a finite thickness (including the wires). Therefore, the sensors could not be sandwiched between sample and pressure plates without creating an air gap.

The initial concept of the temperature measurement was based on utilizing two

4. Measurement of through-plane thermal conductivity

aluminum plates of 3 mm thickness and same cross-section area (x-y plane) as the sample. Those were then used to sandwich the sample. In addition, a channel was machined up to the center in both plates which is illustrated in Figure 4.1. The depth of the channels was such that the PT100 sensors (along with connecting wires) can be accommodated completely within the channel. These two plates along with sensors were then stacked on both sides of the sample and then mounted in the calorimeter. The idea was that each PT100 would be able to measure the surface temperature of the sample on both sides.

A sample made from an acrylic glass sheet of 2 mm was fabricated which had an isotropic thermal conductivity of $0.19 \text{ W m}^{-1} \text{ K}^{-1}$, which is in the order of the expected Li-ion battery through-plane thermal conductivity value ($<1 \text{ W m}^{-1} \text{ K}^{-1}$). However, the expected temperature drop was not obtained. One of the possible reasons could be that the heat flow through the sample area was dominantly along the z-direction and the PT100 (along with wire) was itself offering a high resistance path for the heat to flow.

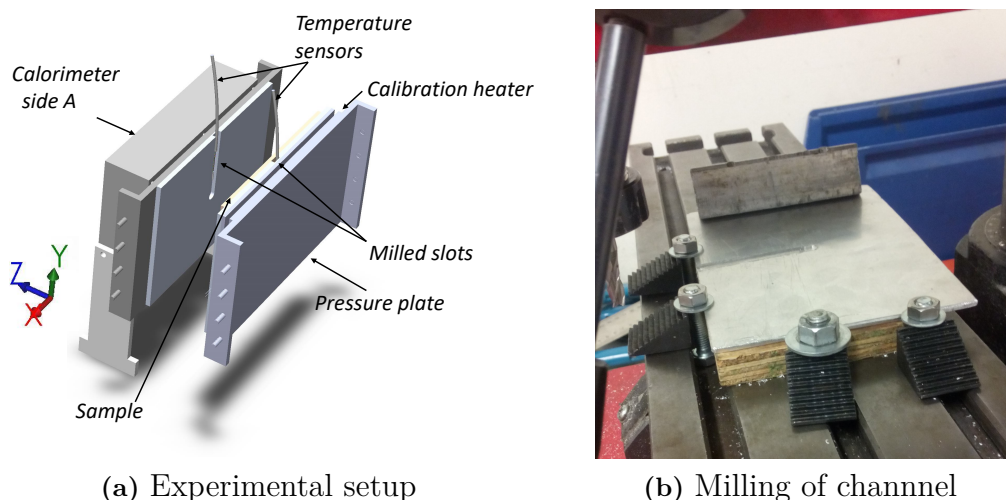
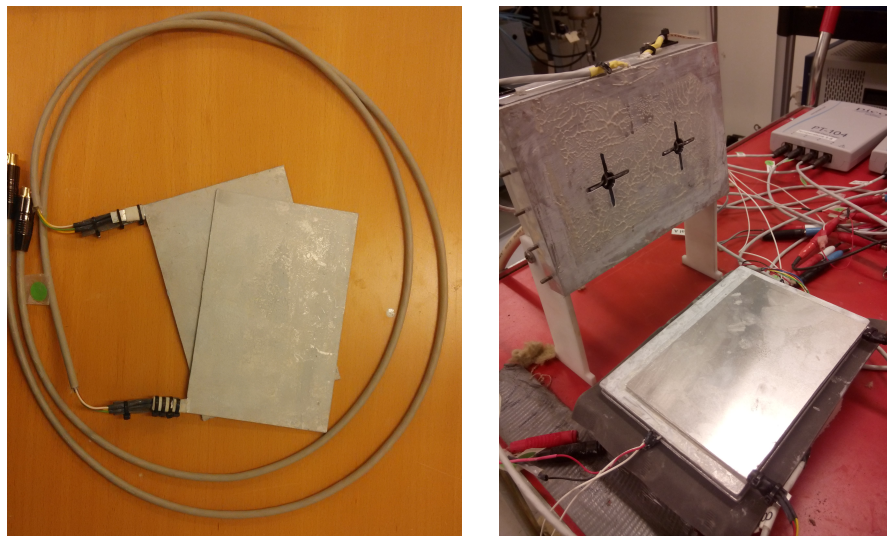


Figure 4.1: Initial concept for through-plane conductivity measurement

This issue was overcome by fabricating plates made from aluminum of similar cross-section area (x-y plane) as the sample and thickness 0.5 mm (z-direction). The PT100 sensor was then mounted on a small extension from each aluminum plate as shown in Figure 4.2. The PT100 sensors were placed close to the sensing area of plates and secured with ties to the extension so as to prevent displacement during handling. The method was again applied for acrylic glass samples for validation of the method.

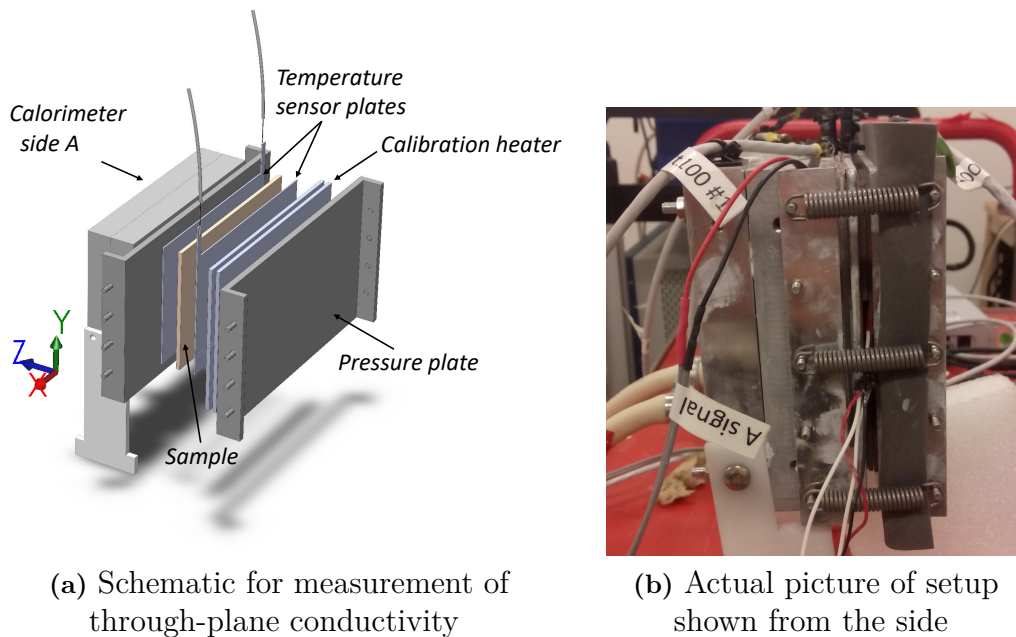
4.2 Validation

The experiment was carried out for an acrylic sheet of cross-section area 0.015 m^2 , thickness 2 mm and repeated for a sandwich of 3 sheets (6 mm in total). The setup



(a) PT100 sensors mounted close to the sensing area (b) Assembly with sample

Figure 4.2: Fabricated temperature sensing plates from 0.5 mm thick aluminum assembly can be seen in Figure 4.3.



(a) Schematic for measurement of through-plane conductivity (b) Actual picture of setup shown from the side

Figure 4.3: Through plane conductivity experiment

The heat flow as well as the temperature difference over the sample stabilizes after sufficiently long time as can be seen in Figure 4.4. The time to reach steady state is dependent on the specific heat capacity of sample and will vary between different sample materials. The results of the test by utilizing (4.1) are shown in Table 4.1. The presented power levels are based on application of constant current levels (0.5 A & 0.7 A) to the heater. However, the represented value is the converted steady state

4. Measurement of through-plane thermal conductivity

voltage sensed by the heat flow sensors during the experiment and not to be confused with applied power to the heaters. The measurement uncertainty for this method was calculated to be $\pm 3\%$ and is shown in Appendix A.2.

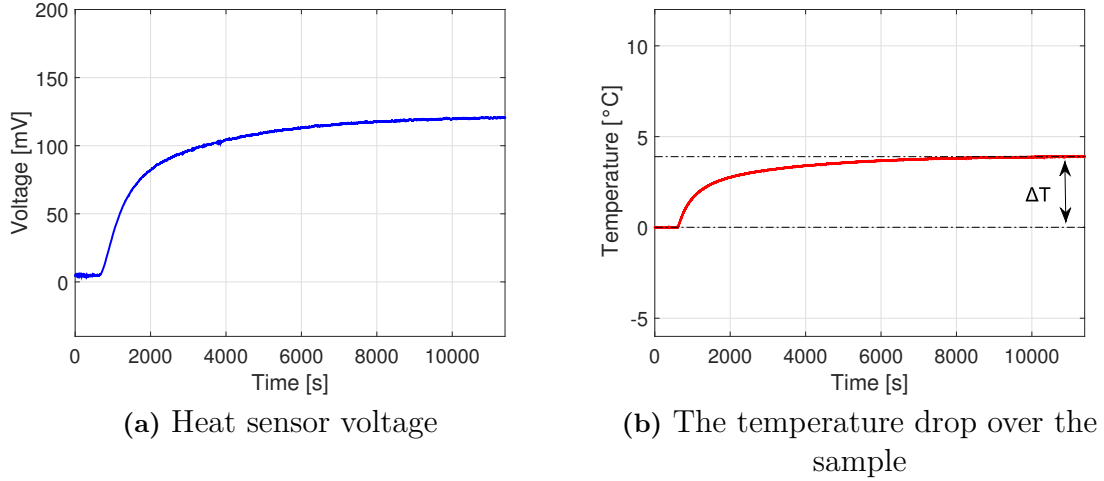


Figure 4.4: Measurements of the through-plane conductivity of sample

Since each experiment takes significant time for completion, the number of tests on the sample were limited. Another issue faced by prolonging the experiment was that the cooling arrangement of pump and water reservoir began to see an increase in temperature ($\approx 0.1^\circ\text{C}$), as the experiment was continued for sufficiently long time. The results from the experiments were acceptable to validate the method. This method of testing was utilized for measurement on Li-ion cells.

Table 4.1: Through-plane conductivity experiment for reference material (i.e. Acrylic glass with isotropic $k = 0.19 \text{ W m}^{-1} \text{ K}^{-1}$)

Sample	Power [W]	ΔT [$^\circ\text{C}$]	k_z [$\text{W m}^{-1} \text{ K}^{-1}$]	Error
Acrylic glass sheet	2.21	1.34	0.219	15.2%
Acrylic glass sheet	4.36	2.62	0.222	16.8%
Acrylic glass sandwich	2.04	3.89	0.206	8.4%
Acrylic glass sandwich	3.98	7.35	0.213	12.1%

5

Measurement of in-plane thermal conductivity

In-plane conductivity measurements were conducted by utilizing only one of the calorimeter sides. Firstly, a heater configuration was constructed. Secondly, a new heat flow sensor configuration was assembled to measure the heat flow. Thirdly, the new sensors were calibrated (i.e. retrieval of new ε). Then the method was optimized for good accuracy. Lastly, a modular setup was constructed so that different samples and batteries could be measured more easily. The experiments were carried out both for the x-and y-direction.

5.1 Method development

In Figure 5.1 the initial design for the in-plane conductivity measurement is visualized. Note that the CAD is for the y-direction measurement but the x-direction is similar with a 90° shift of the sample.

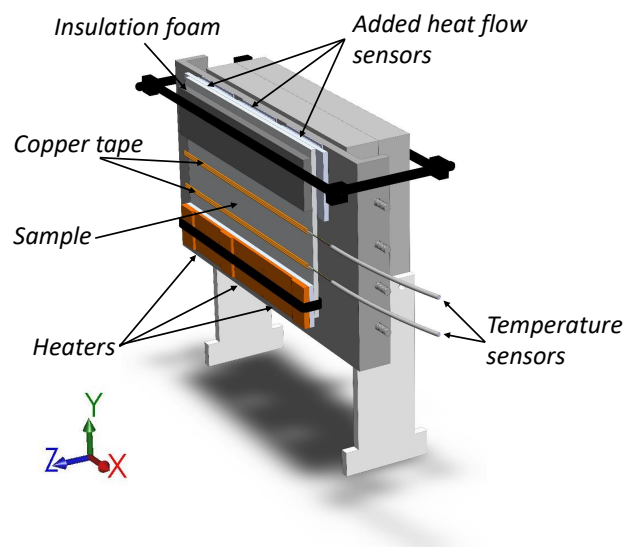


Figure 5.1: CAD schematics of the initial setup of the y-direction in-plane conductivity measurement

In order to replicate the design the different components such as a heater configuration, a heat flow sensor arrangement and a temperature sensor composition had to be designed and manufactured.

5.1.1 Heater configuration

For the in-plane conductivity experiments a new heater configuration was needed in both x- and y-direction. The heat should now be uniform but localized to a certain part of the sample or battery. Also, in order to measure the input power in an accurate way, four-wire measurements of the voltage were utilized similarly to what was described in section 3.3.2. Three heater mats with the dimensions 25 x 50 mm and nominal power 1.25 W were used for the y-direction and only two for the x-direction. They were mounted on 3 mm thick aluminum pieces with the dimensions 25 x 150 and 25 x 100 respectively in order to spread the heat uniformly. The configurations can be seen in Figure 5.2 with their placement and the electrical connections.

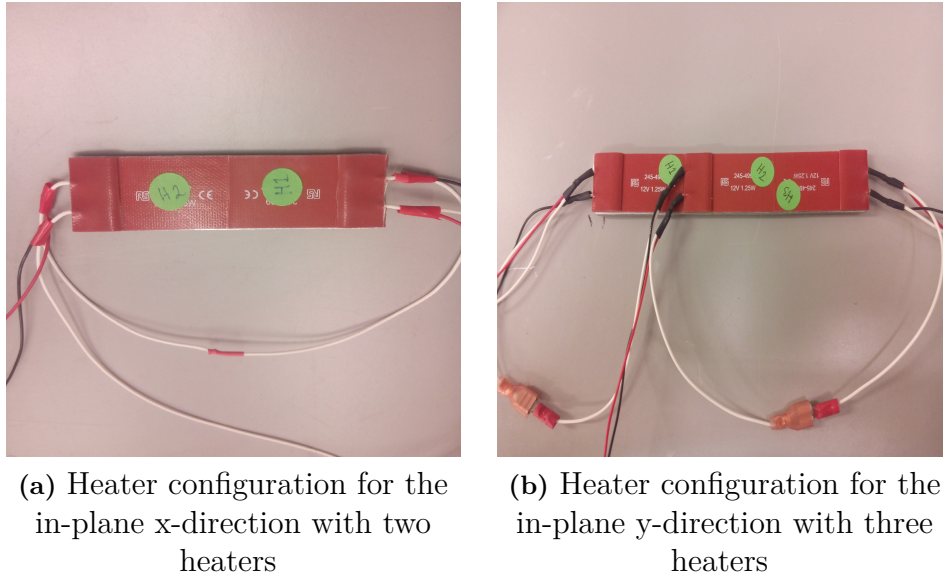


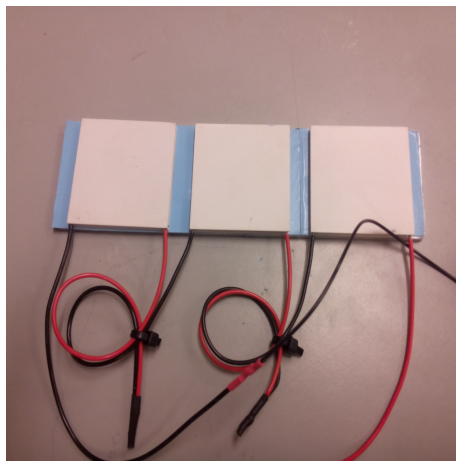
Figure 5.2: Heater configurations for the in-plane conductivity measurements.

The heater mats nominal voltage were same as for the calibration heater, 12 V, which meant that voltage dividers had to be utilized to map the voltage. Two different high precision resistors were used to construct each voltage divider. Slightly different values were used compared to the previous voltage divider (see section 3.3.2) which resulted in the following mapping voltage for each heater mat:

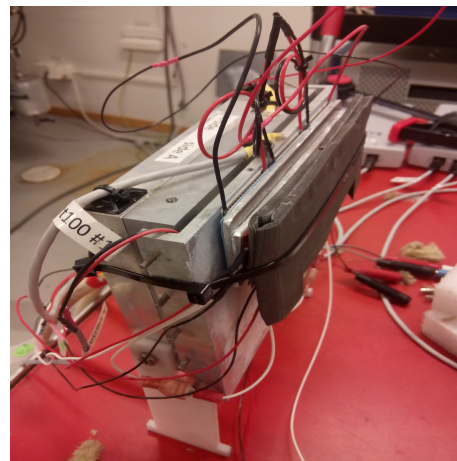
$$V_{aux} = V_{act} \frac{R_1}{R_1 + R_2} = 12 [V] \frac{24.9 [k\Omega]}{51.1 [k\Omega] + 24.9 [k\Omega]} = 3.93 [V] \quad (5.1)$$

5.1.2 Heat flow sensor configuration

In order to measure what heat that actually transferred through the sample a new heat flow sensor configuration had to be constructed. A 3 mm aluminum piece was used as backing and the heat flow sensors were put with their hot side against the sample and the cold side against the calorimeter pressure plate. The three sensors were then series connected before mounting them with a thermal pad onto the aluminum as can be seen in Figure 5.3a. This heat flow sensor arrangement was utilized for both x- and y-direction.



(a) Heat flow sensor configuration utilized for both x- and y-direction.



(b) Photo of the actual calibration setup.

Figure 5.3: The new heat flow sensor configuration as well as the setup during calibration of the sensors.

Since this was a new configuration of heat flow sensors a calibration had to be conducted. The y-direction heater (described in section 5.1.1) was attached directly onto the heat flow sensor arrangement which in turn were attached onto the calorimeter pressure plate as can be seen in Figure 5.3b. In order to control the conditions from time to time and improve the insulation of the setup a new glass-wool insulated box was constructed. After putting the setup in the insulated box the sensors were calibrated with two different currents: 0.061 A and 0.081 A which corresponds to 1.3 W and 2.16 W respectively. By utilizing the calibration concept in 2.3.1 the new calibration constant ε_2 could be calculated to 17.382 W V⁻¹ and 17.381 W V⁻¹ respectively (see Table 5.1).

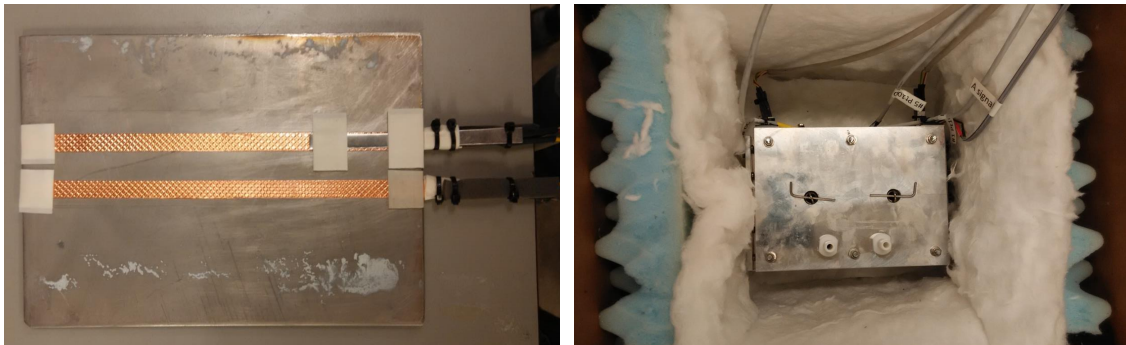
Table 5.1: Measurement values from the steady-state calibration tests for the new heat flow sensors.

Power [W]	ε_2 [W V ⁻¹]
1.3	17.382
2.16	17.381

By having the setup inside the insulated box it was seen that the variation from time to time as well as the input power did not affect the calibration factor significantly. In addition, by comparing the new calibration factor with the previous one (see section 3.3.3) the difference is comparably small which indicates good and repeatable calibration conditions. Hence, the two different power levels were considered sufficient for retrieval of the new calibration constant.

5.2 Fixed setup

Similarly as for the through-plane conductivity in chapter 4 the one dimensional steady state conduction equation (4.1) was used. Therefore, both the temperature difference and the distance between the temperature sensors were critical for good estimation of $k_{in-plane}$. The experiments were carried out for a reference sample made from Stainless steel (Grade 304L with length x width x thickness: 151mm x 102mm x 2 mm respectively). The grade SS 304L has an isotropic thermal conductivity of $14.76 \text{ W m}^{-1} \text{ K}^{-1}$ as given in [31]. Stainless steel was chosen since it would result in a few degrees in temperature difference. The alternatives were aluminum (resulting in a fraction of a degree) or acrylic glass (resulting in several hundred °C). Moreover, since the temperature measurement on a discrete point of the sample would not have been representative for the full length the initial setup (see Figure 5.4a) had copper tape wound around the sample. The PT100 sensors were then taped at the edge of the sample in contact with the tape. Short aluminum strips were also added for better mechanical strength.



(a) Photo of the prepared sample with copper tape to spread the heat for the PT100 measurement on the edge. (b) Photo of the setup inside the new insulation box. The lid is not visible but is also insulated with glass wool.

Figure 5.4: Photos of the initial setup for the in-plane conductivity measurements.

Finally, the experiment was conducted as per the CAD schematics in Figure 5.1. When the sample had been mounted and put in the insulation box (see Figure 5.4b) the in-plane conductivity could be calculated from the measurement data. The resulting conductivity for an input power of 2.16 W was $15.3 \text{ W m}^{-1} \text{ K}^{-1}$ which was

close to the reference value of 14.76 with an error of 3.8%. However, the modularity and preparation time were practical issues. It was realized that the issue of repeatedly placing the tape and PT100s at the exact distance would be impractical for applying on actual battery cells. Also, the time for making the initial assembly was too long. Therefore, a modular setup that preferably would achieve the same accuracy, had to be designed and manufactured.

5.3 Modular setup

In order to overcome the obstacle of being impractical and non-repeatable, an arrangement similar to the CAD schematics in Figure 5.6a was the new aim. Firstly, it was desirable to keep the two temperature sensors at a certain distance. This was achieved by manufacturing two thin bars with 20 mm long spacers and attaching the sensors at a known position onto the bars. Secondly, as the temperatures should represent the whole width of each bar and not only discrete points, a heat-spreading copper tape was applied onto each bar. The arrangement can be seen in Figure 5.5a.

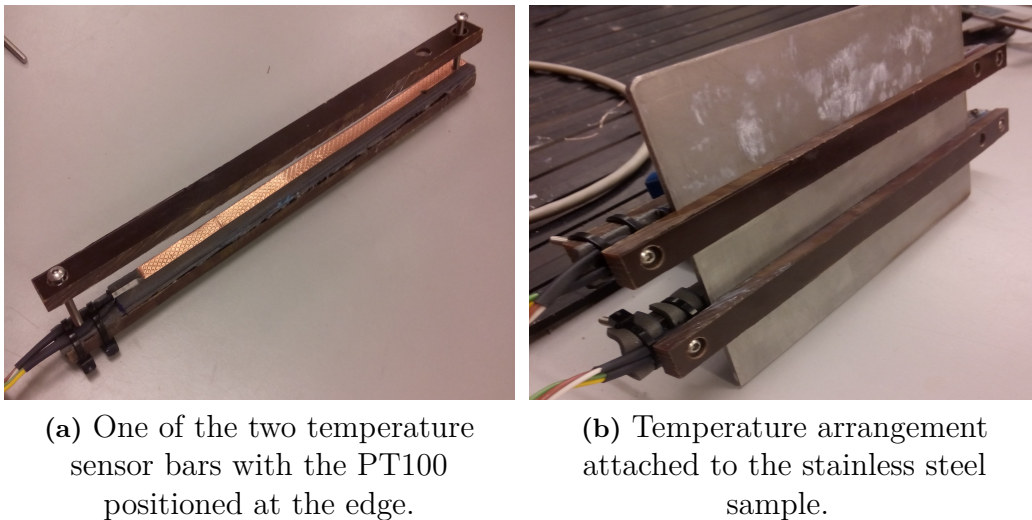


Figure 5.5: Temperature sensor arrangements as where the heat spreading copper tape is visible in the single sensor bar photo (a) and the final sample assembly (b).

In addition, the heat sensors were glued onto the insulating foam backing and tightened with ties to get better stability. The two bars were then used to clamp the PT100 sensors onto the sample as in Figure 5.5b.

By fastening all the components with screws and bolts it was possible to make changes more easily and to utilize for different samples. Moreover, in order to be sure that most of the heat would be transferred through the sample it was desired to have an airgap between the heater side and the calorimeter. The modular setup was designed so that an airgap of 2 mm (see Figure 5.6b) was obtained and that the only part in contact with the calorimeter would be the heat flow sensor arrange-

5. Measurement of in-plane thermal conductivity

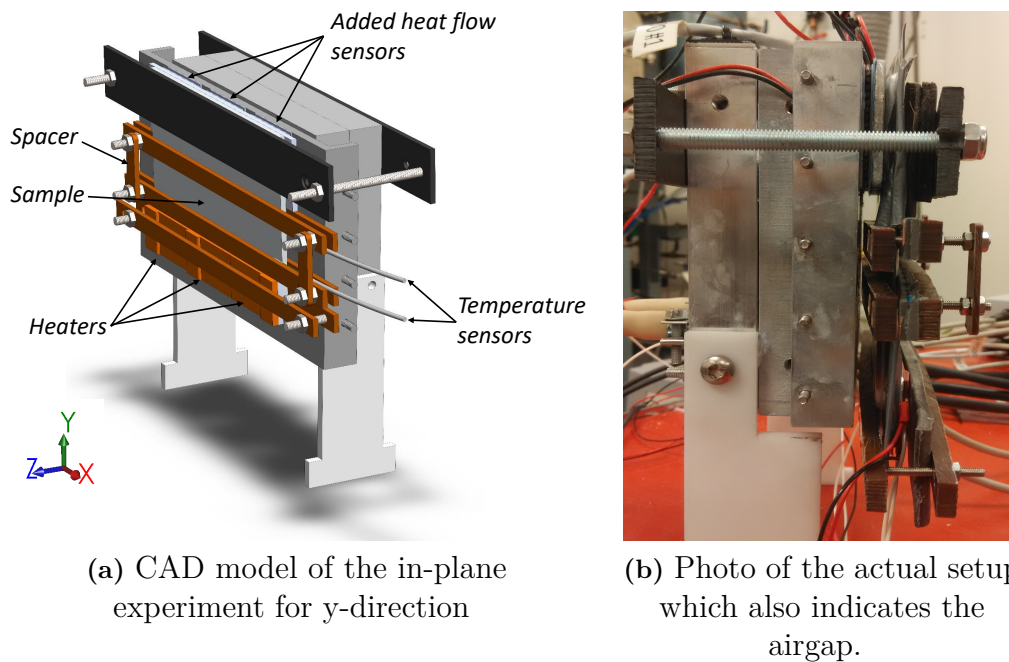


Figure 5.6: Experimental setup for the in-plane conductivity measurements.

ment. Finally, the measurement data could be retrieved and is shown in Figure 5.7 for an input power of 1.3 W. It can be seen that steady state was achieved after approximately 3 h.

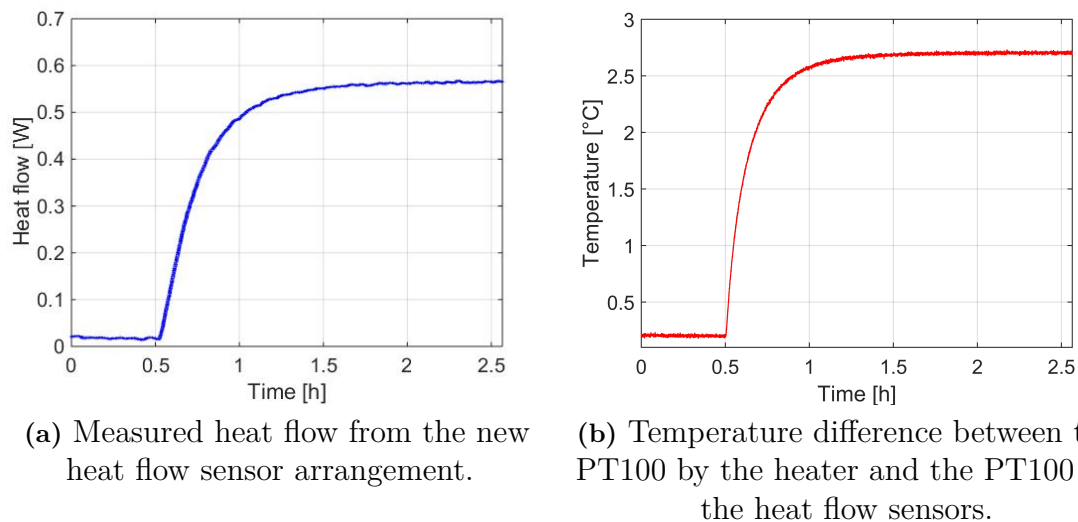


Figure 5.7: The heat flow rate as well as the temperature difference for the measurement of stainless steel.

With the new cross-section area (compared to through-plane conductivity) of 2 x 151 mm and the achieved heat flow and temperature difference curves the in-plane conductivity could be calculated. The results of the experiments are summarized in the Table 5.2.

Table 5.2: In-plane conductivity experiment for reference material (i.e SS 304L $k_{iso} = 14.76 \text{ W m}^{-1} \text{ K}^{-1}$) with a calculated measurement uncertainty of 3.3 %.

Power [W]	k_y [$\text{W m}^{-1} \text{ K}^{-1}$]	Error
1.32	14.47	2.0 %
1.32	14.58	1.2 %
2.16	14.82	0.4 %
2.16	14.76	0.0 %

Since the stainless steel sample is isotropic it was unnecessary to validate the method in x-direction as well.

6

Measurement of specific heat capacity

This chapter describes the method development for measurement of specific heat capacity. Several approaches were attempted, such as a dynamic method, before converging onto preferred method of absorbed heat measurement. The validation results of this method are presented at the end of the chapter.

6.1 Method development

Several methods were investigated for the measurement of specific heat capacity. Most of them were based on adiabatic conditions during the experiment and applying a known amount of heat while measuring the temperature rise of the sample. However, it was found to be very difficult to isolate the system completely from the ambient temperature fluctuations.

6.1.1 Dynamic method

A significant challenge in the experimental setup design as per theory for specific heat capacity was to restrict heat losses while the material shows a temperature response. Therefore, this theoretical approach to experiment design was changed as per the IHC response to heat input.

The use of an isothermal conduction calorimeter for measurement of specific heat capacity has been investigated by Löwen et al.[9]. The methodology for calculation of the specific heat is based on measurement of the first time constant of the calorimeter τ_1 , from a two time constant dynamic correction (see (2.16)). This first time constant was measured for three cases: calorimeter without any sample (denoted as τ_0), a known reference material in the calorimeter (denoted as τ_{ref} and the experiment sample (whose specific heat capacity is to be measured, denoted as τ_{exp}). The specific heat capacity for the sample material was evaluated as per Equations (6.1) to (6.3).

$$\Delta\tau_{ref} = \tau_{ref} - \tau_0 \quad \text{and} \quad \Delta\tau_{exp} = \tau_{exp} - \tau_0 \quad (6.1)$$

$$\Delta\tau_{ref}^* = \frac{\Delta\tau_{ref}}{m_{ref}} \quad \text{and} \quad \Delta\tau_{exp}^* = \frac{\Delta\tau_{exp}}{m_{exp}} \quad (6.2)$$

$$C_{p,exp} = C_{p,ref} \cdot \frac{\Delta\tau_{exp}^*}{\Delta\tau_{ref}^*} \quad (6.3)$$

where, $\Delta\tau_{ref}$ is the difference between the first time constant of the known reference material and the calorimeter, m_{ref} is the mass of known reference, $\Delta\tau_{exp}$ is the difference between the time constant of the experiment sample and the calorimeter, m_{exp} is the mass of the sample.

For this experiment, the reference sample was fabricated from an aluminum sheet (3 mm thickness) of known specific heat capacity of $900 \text{ J kg}^{-1} \text{ K}^{-1}$. The experiment sample was Stainless Steel SS304L (2 mm thickness). The first time constants for aluminum and SS304L samples, τ_{ref} and τ_{exp} respectively, were calculated after carrying out experiments. Finally, the first time constant τ_0 for the calorimeter without any sample inside it was calculated and (6.3) was utilized to calculate the specific heat of stainless steel. However, this method was not successful. One of the possible reasons for high errors can be that this method (2.16) is only applicable when the heat generation occurs at the center of the calorimeter whereas in this experiment, the calibration heater can be placed on one side of the sample. This will alter the second time constant τ_2 , which signifies the internal temperature gradient within the sample [9], and consequently the measured first time constant τ_1 may not be representative of its true value.

6.1.2 Absorbed Heat Method

In the next approach, instead of applying heat and measuring the response of the sample, a known temperature rise was applied to the calorimeter by changing the temperature of cooling water in the heat sinks. Consequently, the heat absorbed by the system was measured from the negative voltage output of calorimeter. A similar approach was conducted previously by Bazinski et al.[8] which is kept as reference. The general setup of calorimeter was modified for the measurement of specific heat capacity.

The calorimeter side B was removed and the sample material was placed in between the pressure plates as seen in Figure 6.1. The temperature of the sample was measured by using the aluminum sensing plates on both sides of the sample. The temperature of the sample at any instant, was defined as the average of the temperatures from both the sensing plates. The whole setup was placed in the insulation box and the temperature of the coolant was regulated using a Julabo F25MA thermal bath [25].

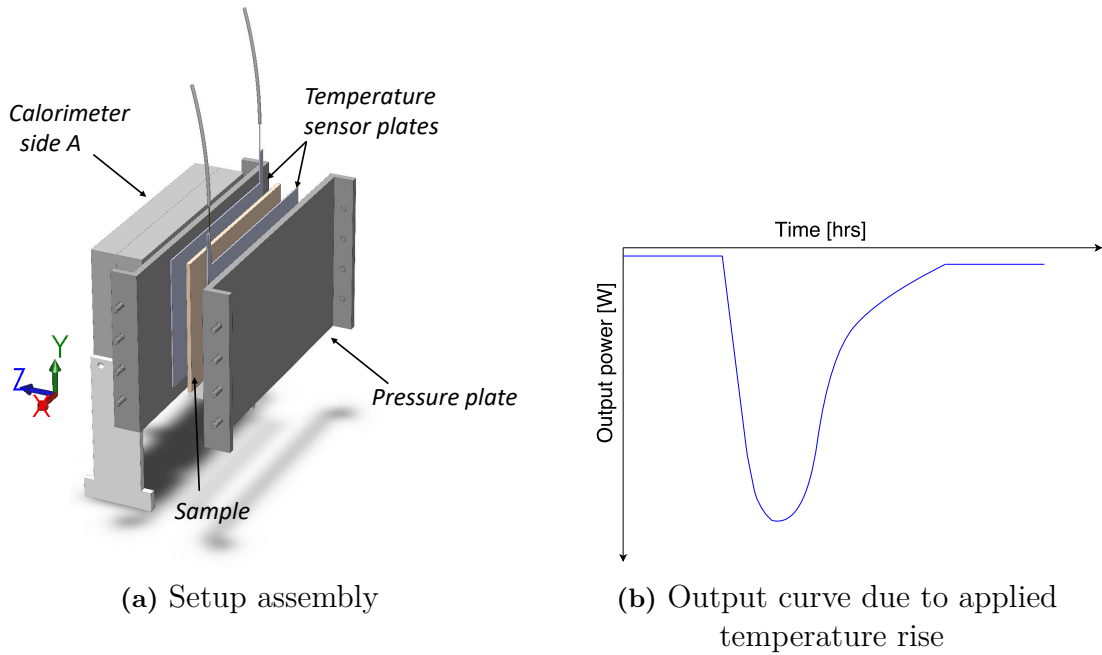


Figure 6.1: Experimental setup for the specific heat capacity measurements.

The output curve obtained from thermopiles was converted to power units (by the calibration coefficient ε) and the curve was integrated to obtain the energy absorbed by the system for the applied temperature rise. Similar experiment was applied for the calorimeter setup without any sample and the absorbed heat was removed from the previous value to correct for the heat absorption by the calorimeter itself. The calculation of the specific heat capacity was done according to

$$C_p = \left(\frac{E - E_0}{m \cdot \delta T} \right) \quad (6.4)$$

where δT is the applied temperature rise, m is the mass of sample, C_p is the specific heat capacity, E is the energy absorbed by sample and calorimeter and E_0 is the energy absorbed by the calorimeter alone.

Issue of the shifting baseline

The setup is maintained at a stable initial temperature for sufficient long time until a baseline is established (labelled as baseline 1 in Figure 6.2). However, it can be observed that after raising the temperature of the setup, the output from heat flow sensors will not return to initial baseline 1, even after allowing enough time for the setup to reach stability. A new baseline is established (labelled as baseline 2 in Figure 6.2). Since the energy absorbed by the sample is given by the area under the curve, it is necessary to correct for this shifting baseline.

The reason for this shift of baseline can be attributed to change in overall temperature of the setup, which affects the equilibrium between the environment and the calorimeter. As the heat transfer equilibrium is dependent on the temperature

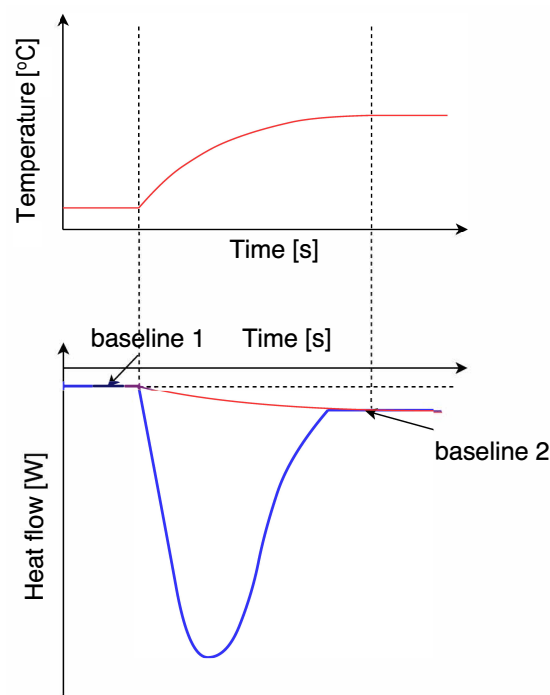


Figure 6.2: Correction of shifting baseline

difference between calorimeter and environment, the correction of the baseline can be carried out as per the surface temperature profile of the calorimeter in Figure 6.2.

6.2 Validation

Measurements of the specific heat capacity were performed as per the methodology described in section 6.1.2. The challenge was to maintain the heat within the setup and keep the same conditions for both the measurement without sample E_0 and the reference measurement with sample E . The results for the C_p measurement for both acrylic glass and aluminum are shown in Table 6.1.

Table 6.1: Resulting specific heat capacity for 5 different measurements.

Sample	Actual value [J kg ⁻¹ K ⁻¹]	Measured value [J kg ⁻¹ K ⁻¹]	Error
Acrylic glass (20-22 °C)	1470	1259	14.3%
Acrylic glass (18-23 °C)	1470	1227	16.6%
Aluminum (20-22 °C)	900	815	9.3%
Aluminum (20-22 °C)	900	907	0.7%
Aluminum (18-23 °C)	900	580	35.5%

The experiments were conducted for two different ΔT i.e 2 °C and 5 °C, to study

the behaviour of the setup. It can be seen that the results for the bigger ΔT of 5°C gave bigger error in the C_p . The aluminum experiment for $\Delta T = 2^\circ\text{C}$ was also repeated to study the repeatability. Since the values varied from time to time it was concluded that the experimental conditions differed for each experiment. The ambient temperature in the room fluctuated by $\approx 4^\circ\text{C}$ and the insulation of setup had to be improved. Thus, an insulated box with finer glass wool and tighter holes for hoses was constructed. This improvement provided more stable conditions during experiment (see Figure 5.4b). The E_0 measurement was repeated for this modified setup as well as for the aluminum sample - both for $\Delta T = 2^\circ\text{C}$ between $(20\text{-}22^\circ\text{C})$. The measurement of the aluminum sample was repeated three times in order to see study the repeatability and the results are summarized in Table 6.2.

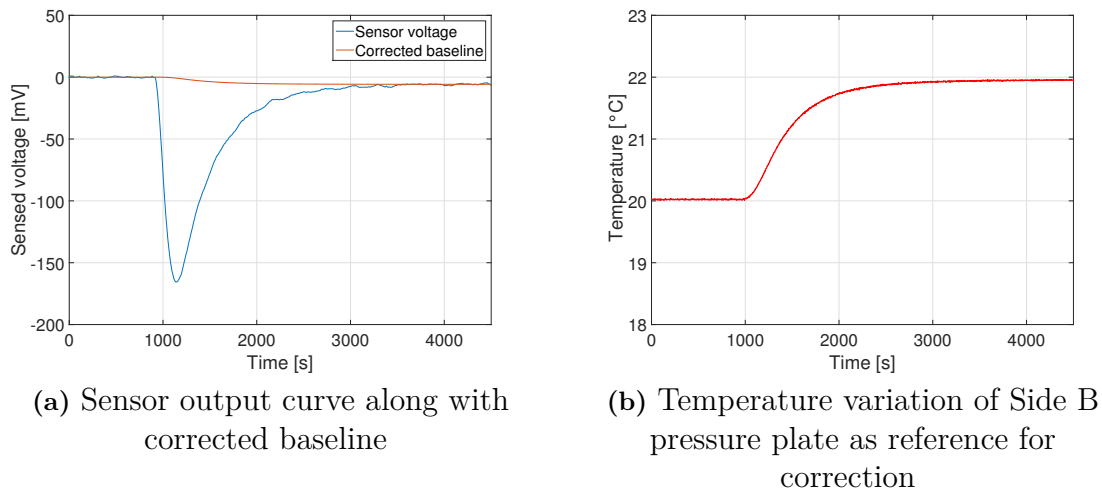


Figure 6.3: Specific heat capacity measurements for aluminum

Table 6.2: Resulting specific heat capacity for three different measurements with improved conditions.

Sample	Actual value [J/kgK]	Measured value [J/kgK]	Error
Aluminum (20-22 °C)	900	949	5.4%
Aluminum (20-22 °C)	900	951	5.7%
Aluminum (20-22 °C)	900	884	1.8%

It can be seen that the error in the calculated C_p -values were reduced and that the absolute range was narrowed. Note that the shifting baseline correction explained in section 6.1.2 was utilized for the calculations. The reference temperature for correction was considered to be Side B pressure plate (Figure 6.3b), since it has the largest surface area which offers more heat transfer to the environment. Moreover, the values could be improved even more, if longer settling time can be provided for the setup. The measured material specific heat capacity values indicate that the method can be utilized for Li-ion cell measurements within acceptable error range ($<10\%$).

6. Measurement of specific heat capacity

7

Battery cell measurements

This chapter conveys the results and analysis of the measurements for the Li-ion cells. The thermal property measurements are presented as well as the heat generation. In addition, a simple simulation model is used to evaluate the experimental results.

Table 7.1: Specification of the two cells used for the experiments - pouch and prismatic.

	Voltage range [V]	Capacity [Ah]	Dimensions (W x H x T) [mm]	Weight [g]	Chemistry
Pouch cell	2.7 - 4.2	6	150x100x6.67	237	NMC
Prismatic cell	2.0 - 3.6	20	173x85x21	636	LFP

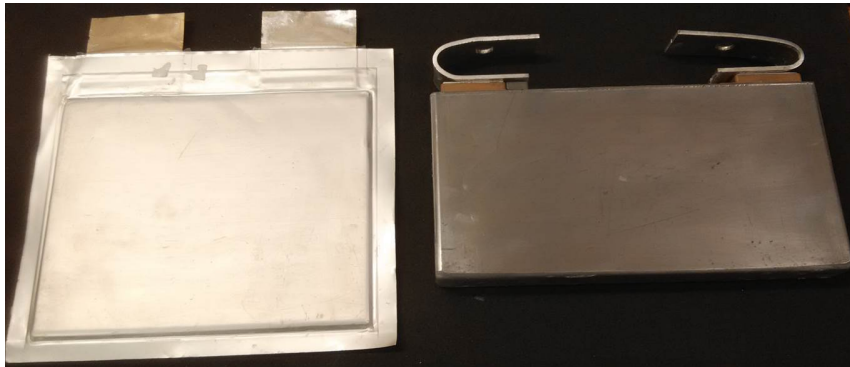


Figure 7.1: Photo of the pouch cell (left) and the prismatic cell (right) used for the experiments.

7.1 Through-plane thermal conductivity

The method described in chapter 4 for measurement of through-plane conductivity was applied for both the Li-ion cell types in Figure 7.1 with specifications as per Table 7.1. In the first experiment, the pouch cell was tested. The measurement was carried out until both heat rate and temperature drop reached steady state. The results of the experiment showed that the value of k_z was calculated

to $0.735 \text{ W m}^{-1} \text{ K}^{-1}$ by utilizing (4.1) and the steady state values from Figure 7.2. This value is typically expected of cells of this type as the heat has to flow through different layers of electrode and separator sheets [3]. The measurement results are summarized in Table 7.2 along with error in the measurement (Appendix A.2).

Table 7.2: Through-plane conductivity experiment for Li-ion pouch cell

Power [W]	$k_z [\text{W m}^{-1} \text{ K}^{-1}]$
2.21	0.735 ± 0.024

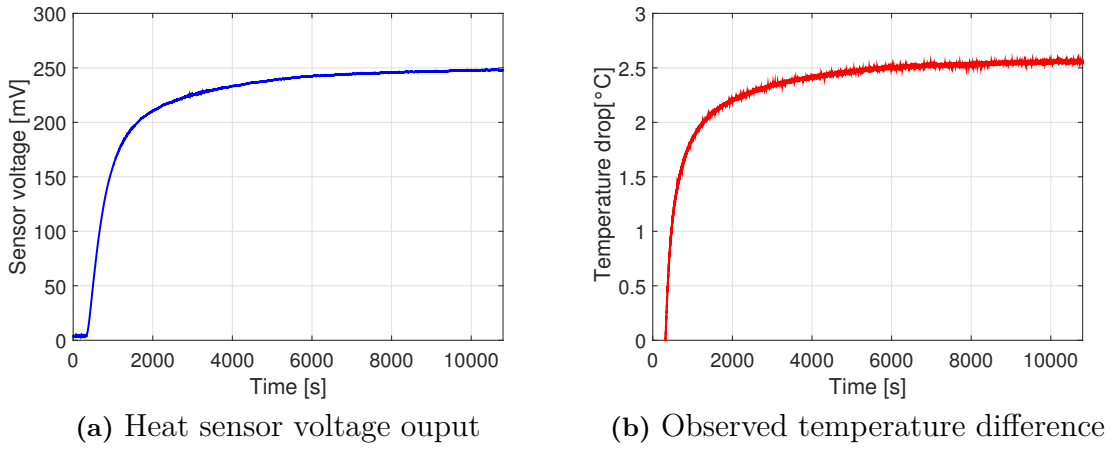


Figure 7.2: Measurement of through-plane conductivity of pouch cell

The method of through-plane conductivity measurement was then applied on the prismatic cell. The results of the experiment showed that the measured temperature difference was very low. The possible reasons for this outcome can be allocated to the very high thermal conductivity of aluminum casing of the cell, which offers the least resistive path to the flow of heat. As the method involves measurement of both temperature and heat flow on the exterior of prismatic cell, the effect of external aluminum casing influenced the result significantly. Alternative methods can be utilized which involve cell disassembly to remove the casing.

7.2 In-plane thermal conductivity

The modular setup method described in section 5.3 was utilized for the pouch cell only and not for prismatic, due to the same reasons as presented in section 7.1.

For the measurement of the in-plane conductivities the fabricated 20 mm spacers was used due to the space limitation in y-direction. The setup for the in-plane y- and x-direction can be seen in Figure 7.3. The temperature sensors were kept as far from the heaters as possible to make measurements in the section where the heat flow becomes uni-directional.

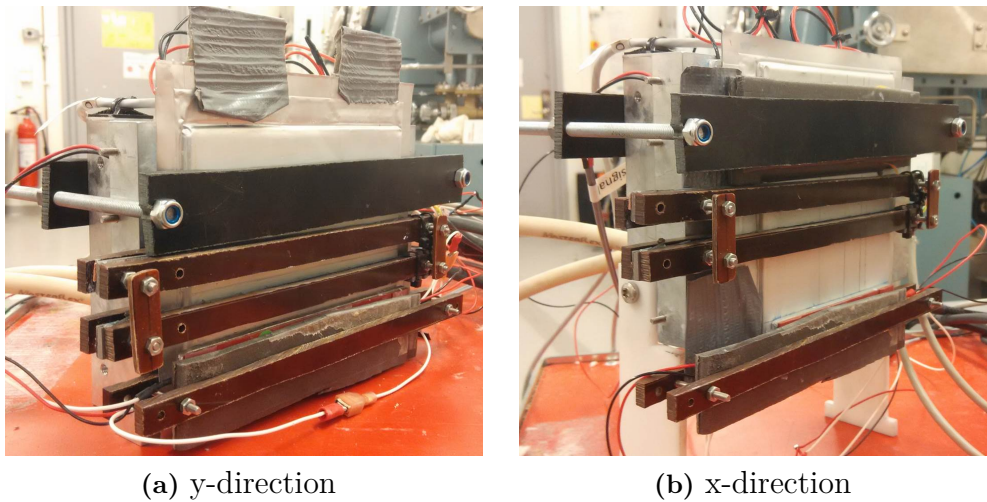
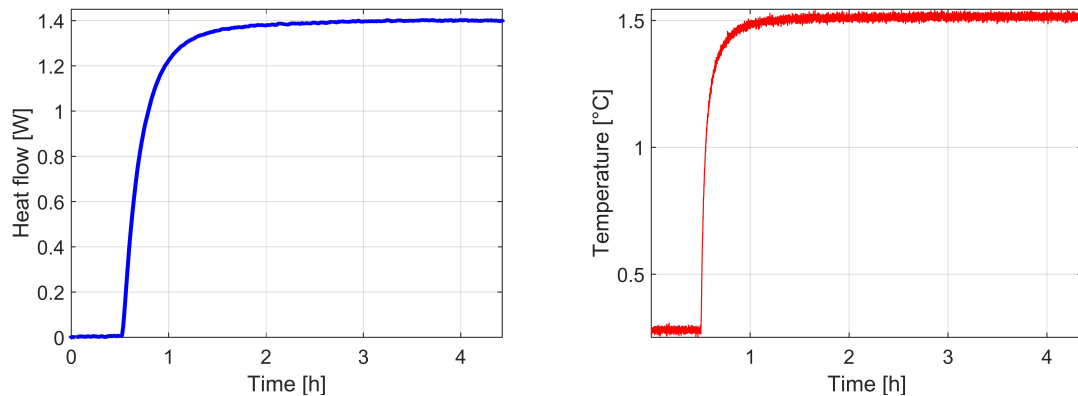


Figure 7.3: Experimental setups for measurement of in-plane conductivities.

The measurements were carried out until both the heat flow and temperature drop had stabilized to a steady state. The steady-state values from Figure 7.4 were then utilized in (4.1) to retrieve the in-plane conductivity.



(a) Measured heat flow through the cell. (b) Observed temperature difference.

Figure 7.4: Measurement of in-plane conductivity of pouch cell

The experiment was conducted for the in-plane x-direction in the same way as for the y-direction but with the battery shifted 90° as is evident from Figure 7.3b. The results for the in-plane conductivities are presented in Table 7.3. It was seen that both the conductivities are significantly larger than the through-plane conductivity as expected. However, a difference between the in-plane conductivities themselves (y-and x-direction) was observed. Usually the two in-plane conductivities are assumed to be the same which may therefore not be true in all cases. The clamping of the electrode sheets as well as other internal composition designs might affect the thermal resistance and consequently the thermal conductivity. The calculated error in the measurements was found to be $\pm 5.4\%$ as shown in Appendix A.3.

Table 7.3: Resulting in-plane thermal conductivities.

Direction	In-plane conductivity	Measurement uncertainty
k_y	23.0 [W m ⁻¹ K ⁻¹]	±1.2
k_x	31.4 [W m ⁻¹ K ⁻¹]	±1.7

7.3 Specific heat capacity

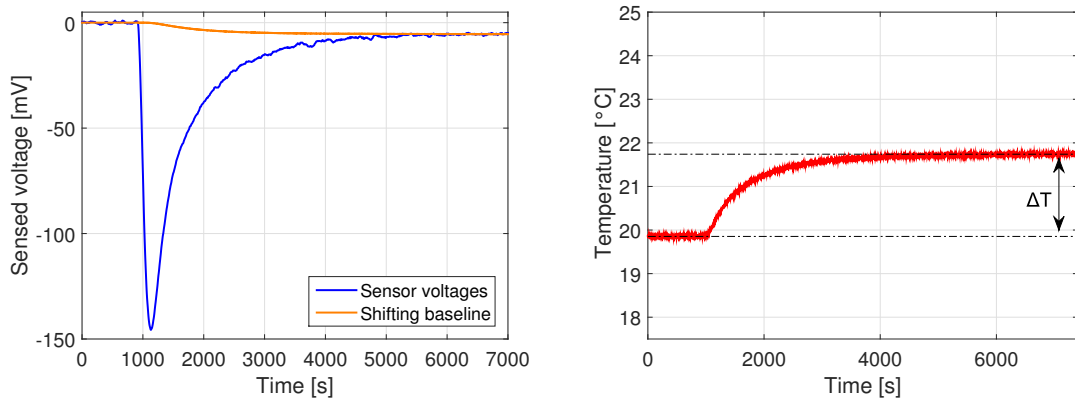
The method of measurement described in Chapter 6 for specific heat capacity was applied on Li-ion pouch and prismatic cells.

In the first step, the energy absorbed by only the calorimeter E_0 , without any sample in it, was evaluated. This value was used in measurements of specific heat capacity of both cell types. In the next step, the pouch cell was mounted in the calorimeter and the energy absorbed was measured. Subsequently, the experiment was repeated for prismatic cell type as well. In all the experiments, the setup was subjected to a temperature rise of 2 °C. This temperature difference ensured that the specific heat capacity did not vary significantly during the experiment.

The measured values of specific heat capacities were 1087 and 1091 J kg⁻¹ K⁻¹ for the prismatic and pouch cell respectively. The values are also presented in Table 7.4 along with error in the measurements (shown in Appendix A.4). In Figure 7.5a the shifting baseline of the heat absorption curve is shown whilst the changing pouch cell temperature is represented in Figure 7.5b. These values of specific heat capacity are around the values for Li-ion cells as reported in literature [7, 8].

Table 7.4: The measured specific heat capacity for the pouch cell and the prismatic cell.

Sample	Measured value [J/kgK]	Measurement uncertainty [J/kgK]
Pouch cell (20-22 °C)	1091	±29.45
Prismatic cell (20-22 °C)	1087	±29.35



(a) The sensor voltage with the shifting baseline. (b) The temperature rise of the pouch cell.

Figure 7.5: Measurements from the specific heat capacity of the pouch cell.

7.4 Heat generation - Pouch cell

In order to investigate the heat generation from the pouch cell during charge/discharge for different C-rates the full calorimeter (both sides) was utilized. The actual electrical connections can be seen in Figure 7.6 where they are tightened onto the cell terminal clamp. The sensing cables were placed close to the feeding cables (not included in the photo).

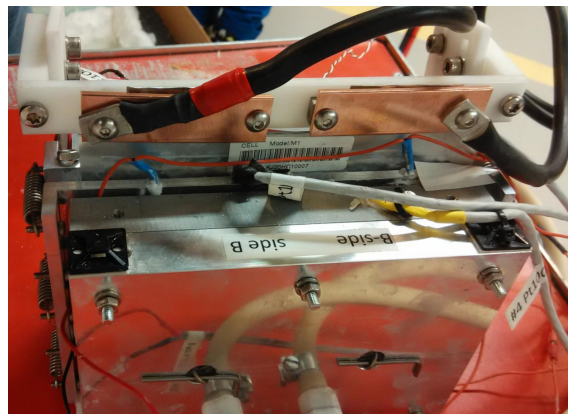


Figure 7.6: Photo of the pouch cell heat generation setup. The sensing cables were connected as close to the feeding cables as possible (not included in photo).

In addition, a temperature sensor was added to the cell as safety cut-off, to shut down the operation if the sensed temperature exceeded 40°C. When the cell had been mounted and connected it was put in the insulation box.

Three different measurements were conducted for the pouch cell: Dynamic, 1.67C discharge/charge and 0.83C discharge/charge. Initially, the capacity of the pouch

7. Battery cell measurements

cell was not known which is why the charge-rates are different from the aim of 1C and 0.5C (assuming a capacity of 10 Ah). Each measurement contained two similar cycles to be able to study the repeatability and to have redundancy. Therefore, all the measurements have calculated values (such as heat generation) for two cycles. The first measurement was the dynamic measurement which contains a very transient load portion and ends with a fast charge. The recorded data is visualized in Figure 7.7 where the following quantities are shown: Cell voltage and fed current; generated power; Tian-corrected generated power and temperature recordings.

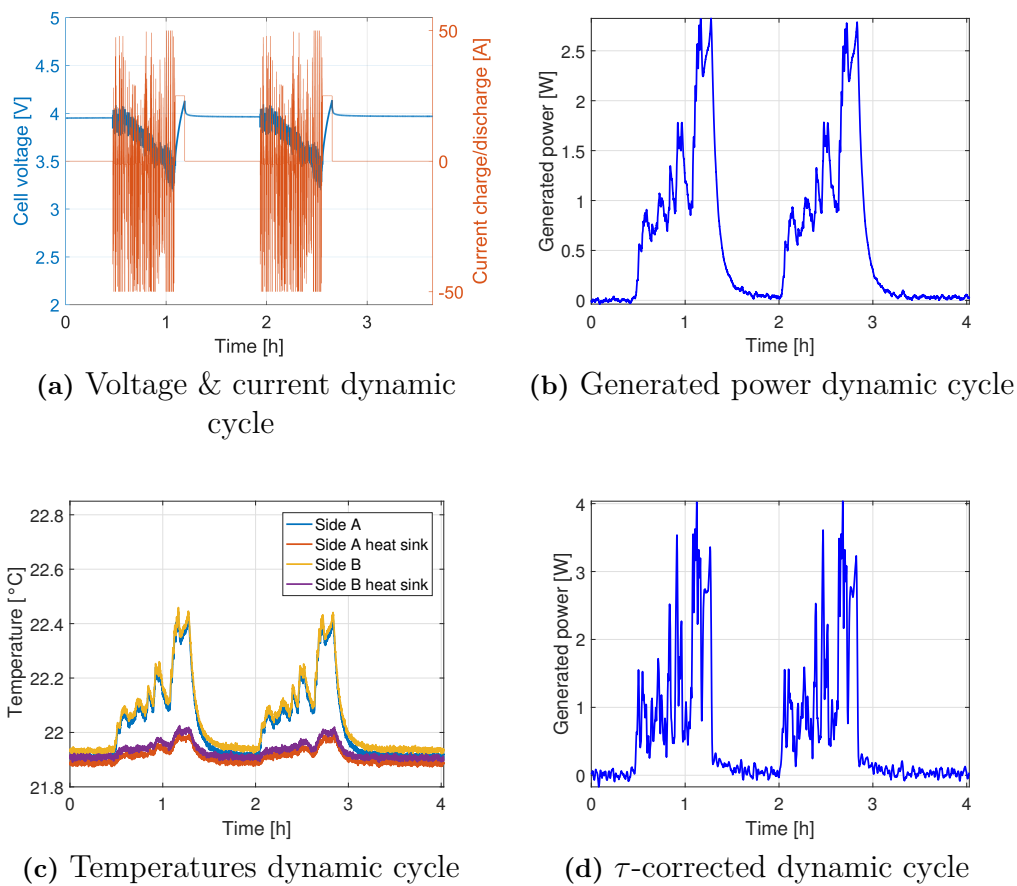


Figure 7.7: The heat generation experimental data for the dynamic cycle. Conducted for the pouch cell.

It can be seen that the transient load portion of the current in Figure 7.7a is reflected both in the temperatures as well as for the heat flow (generated power). However, it can also be observed that the calorimeter, even with the Tian-corrected power, have limitations for the transient portion. The instantaneous generated power may therefore not be exact even if the total amount of energy will be recorded with a delay. From Figure 7.7b and 7.7d it is also evident that the final fast charge generates a lot of heat. Moreover, the Tian-corrected generation shows a higher maximum power than the raw data and since the energy is the same this indicates that a correction is needed. The maximum recorded power for the Tian-corrected generation was 4.04 W and the resulting generated heat for two cycles were 9.05 kJ.

A summary of the heat generation results for the pouch cell (2 cycles) is shown in Table 7.5.

Table 7.5: Summary of the heat generation results for the pouch cell in consideration (2 dynamic cycles).

Pouch cell (2 cycles)	Dynamic cycle
<i>Generated heat [kJ]</i>	9.05
<i>Maximum power [W]</i>	4.04
<i>Average power [W]</i>	0.62
<i>Average power (1 cycle only) [W]</i>	1.35

The two following measurements were designed to contain two cycles of constant discharge and charge of 1C and 0.5C respectively. As mentioned, the capacity was 6 Ah and not the assumed 10 Ah which resulted in the C-rates 1.67C and 0.83C. The same parameters as for the dynamic measurement are visualized in Figure 7.8 as where the discharge/charge current levels are more visible. For the lowest C-rate of 0.83C the noise of the signal began to get more significant which also influenced the Tian-correction since it utilizes the derivative of the data. In addition to what was seen in the dynamic cycle, a bump/plateau is visible for the two different C-rates in the middle of the discharge and charge. Since the heat flow as well as the temperatures levels out or even drop this reaction has to be endothermic and absorbs energy. The difference between charge and discharge shows that the endothermic reactions are more evident in the charge-process. If the irreversible losses are sufficiently small the reversible heat rate (described in section 2.2) can be observed and even quantified. If the encircled portions in Figure 7.8d are assumed to be at the same SOC level this could be used to approximate the reversible heat rate. The difference between the two encircled instants (the drop in power) is approximately 0.4 W which means that if the irreversible heat rate is assumed constant ($I \cdot R = const.$) the reversible heat rate is:

$$\begin{cases} \text{Discharge : } Rev + I \cdot R = 0.4 \text{ W} \\ \text{Charge : } -Rev + I \cdot R = 0 \end{cases} \Rightarrow Rev = 0.2 \text{ W} \quad (7.1)$$

A summary of the heat generation results for the pouch cell is presented in Table 7.6 as were it can be seen that the generated heat for the discharge portions dominates over the charge portions.

7. Battery cell measurements

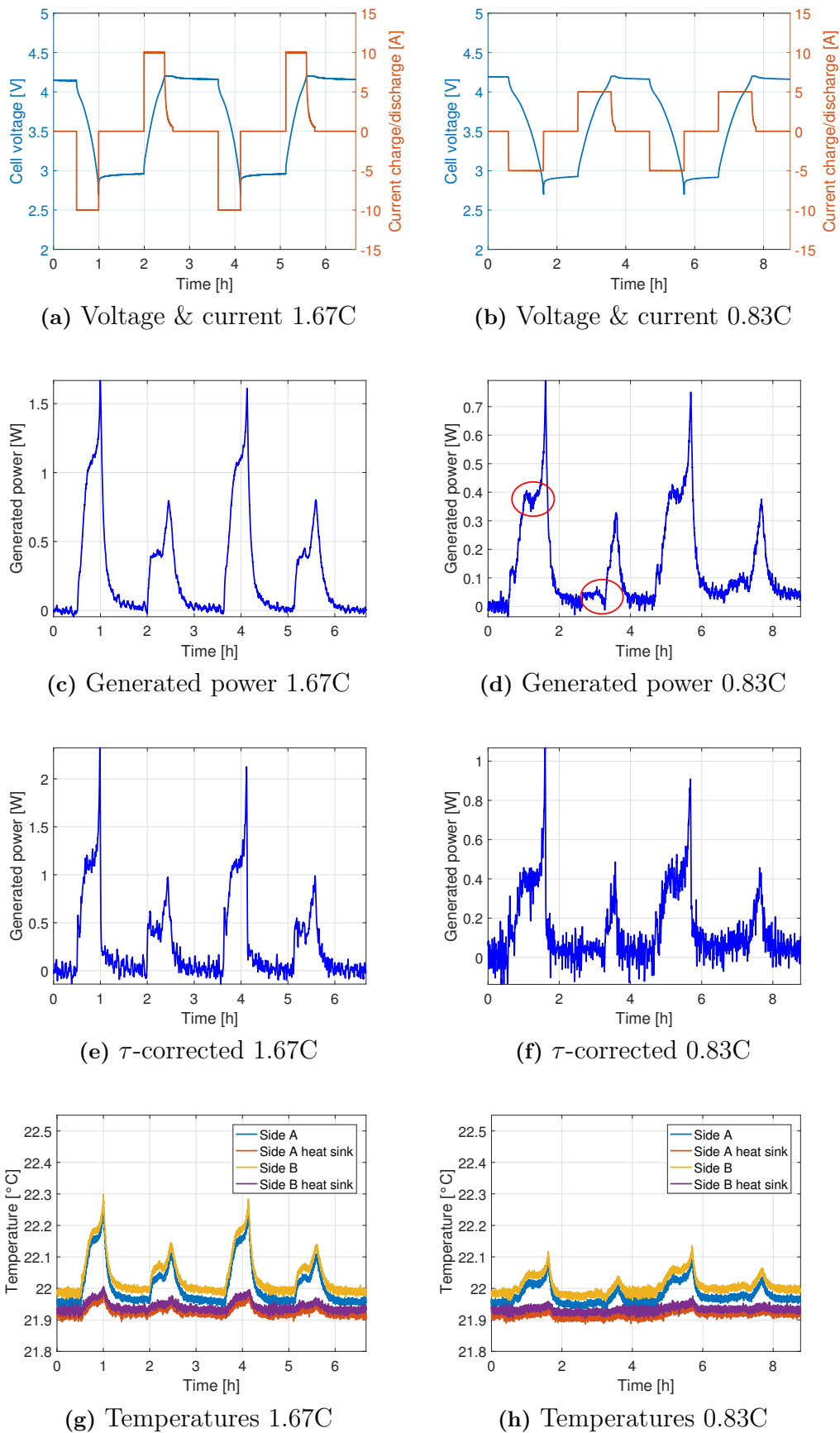


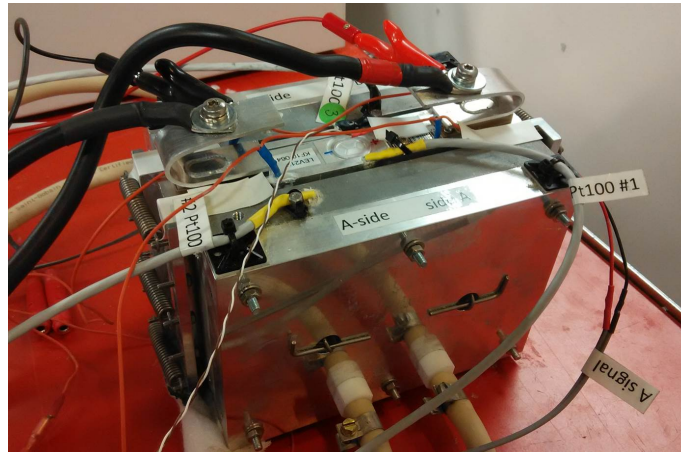
Figure 7.8: The heat generation experimental data for the 1.67C and 0.83C discharge/charge cycle. Conducted for the pouch cell.

Table 7.6: Summary of the heat generation results for the pouch cell (2 discharge/charge cycles).

Pouch cell (2 cycles)	1.67C Discharge/ Charge	0.83C Discharge/ Charge
<i>Generated heat [kJ]</i>	6.52	4.46
<i>Maximum power [W]</i>	2.32	1.07
<i>Average power [W]</i>	0.27	0.14
<i>Average power (1 discharge) [W]</i>	0.73	0.27
<i>Average power (1 charge) [W]</i>	0.42	0.16

7.5 Heat generation - Prismatic cell

The heat generation measurements were also conducted for the prismatic cell. Since the terminal electrodes were much more stable for the prismatic cell, no clamps were needed. The electrical connections can be seen in Figure 7.9 as well as the thermocouple which was attached similarly as for the pouch cell. This temperature measurement was simply a security measure to shut down if the cell was overheated.

**Figure 7.9:** Photo of the prismatic cell heat generation setup.

The prismatic cell was then put in the insulation box and was subjected to similar load cycles as the pouch cell. The measurement data for the dynamic measurement is shown in Figure 7.10 as where it is obvious that the generated heat is high compared to the pouch.

7. Battery cell measurements

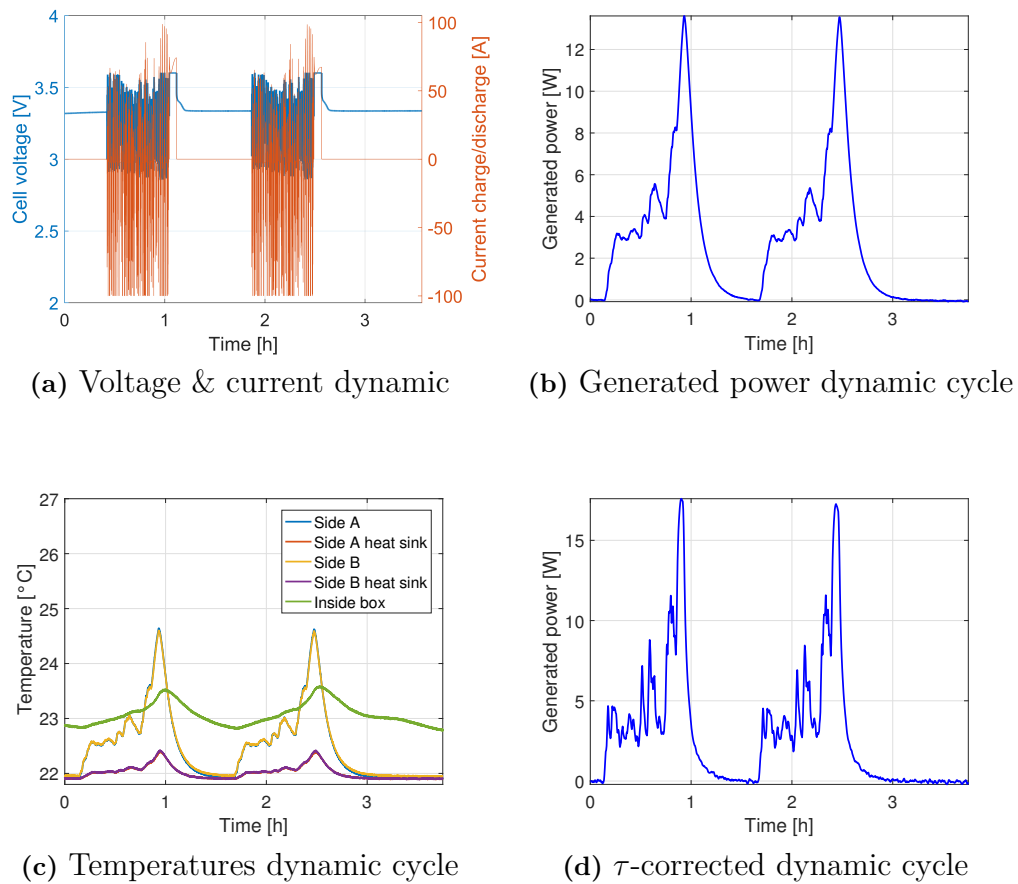


Figure 7.10: The heat generation experimental data for the dynamic cycle. Conducted for the prismatic cell.

The maximum power recorded for the dynamic measurement was 17.6 W and the total generated heat for the two cycles was 38.2 kJ (see Table 7.7). It can be concluded that the cell impedance has a significant impact on the heat generation due to the Ohmic losses. As was presented in section 2.1.2 the irreversible losses are greatly affected by both the current and the impedance.

Table 7.7: Summary of the heat generation results for the prismatic cell (2 dynamic cycles).

Prismatic cell (2 cycles)	Dynamic cycle
<i>Generated heat [kJ]</i>	38.2
<i>Maximum power [W]</i>	17.6
<i>Average power [W]</i>	2.83
<i>Average power (1 cycle only) [W]</i>	3.79

The two constant discharge/charge experiments were conducted for the C-rates 1C and 0.5C. The measurement data is visualized in Figure 7.11.

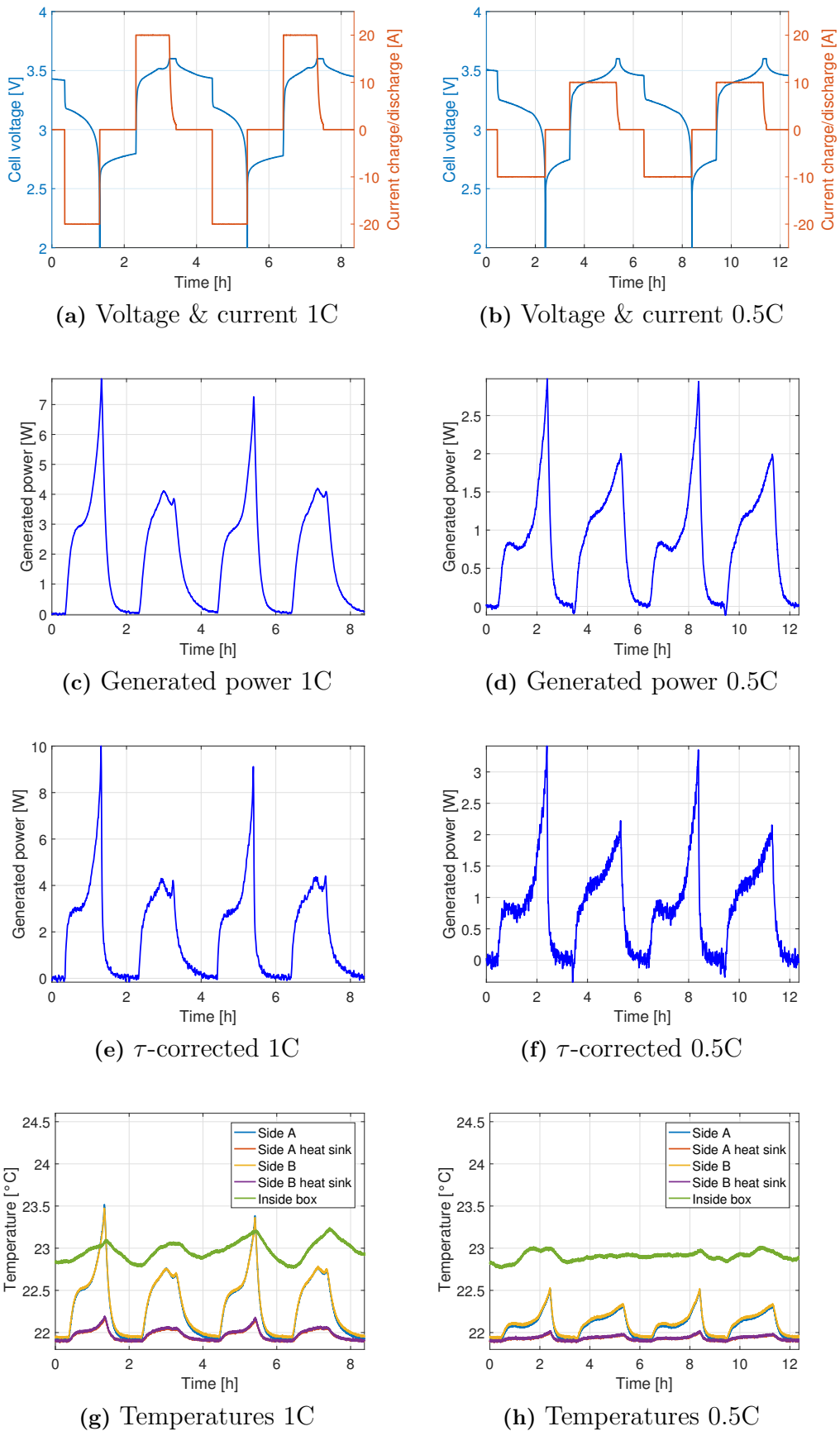


Figure 7.11: The heat generation experimental data for the 1C and 0.5C discharge/charge cycle. Conducted for the pouch cell.

It should be observed that the cell voltage drops fast when approaching low SOC and that the average discharge and charge power are more or less equal for the 0.5C case. Furthermore, the "inside box" temperature was added for the prismatic cell measurements. It was not included for the pouch because then the calorimeter temperatures would not be visible. However, this PT100 sensor shows how the temperature inside the box is varying during the experiments which can explain the somewhat varying peaks from one discharge to another. If the surrounding temperature of the calorimeter is not same during an identical discharge or charge the heat flow will not be equal either. To improve the heat generation measurements further the insulation of the setup (now the insulated box) should be improved. Ideally, all the generated power from the cell should be transferred away to keep the same baseline throughout each experiment and cycle. A summary of the heat generation results for the prismatic cell is presented in Table 7.8.

Table 7.8: Summary of the heat generation results for the prismatic cell (2 discharge/charge cycles).

Pouch cell (2 cycles)	1C Discharge/ Charge	0.5C Discharge/ Charge
<i>Generated heat [kJ]</i>	57.1	36.2
<i>Maximum power [W]</i>	10.0	3.41
<i>Average power [W]</i>	1.89	0.81
<i>Average power (1 discharge) [W]</i>	2.61	1.01
<i>Average power (1 charge) [W]</i>	2.06	1.02

7.6 Simulation model

In order to evaluate what temperature distribution $T(x, y, z)$ there is within the battery, and consequently maximum temperature in hot-spots, a three dimensional model was made in COMSOL multiphysics. The module "Heat transfer in solids" was utilized with a time-dependent study in 3D. Moreover, the measured thermal properties were utilized as inputs for the battery model. The heat conductivities (k_y, k_x, k_z) were implemented in their respective direction as well as the measured weight and specific heat capacity (see Table 7.9). It should be noted that the accuracy of the model and the results should solely be seen as indications and proof of concept.

Several simplifications were applied to the modelling of the pouch cell battery. First, the pouch cell battery was simplified to a cuboid and the meshing can be seen in Figure 7.12a. The minimum quality factor was 0.6 whilst the average quality factor was 0.8. This was considered as a sufficiently good mesh as a proof of concept even if an enhanced mesh would give a better representation of the solid cuboid. However, this would increase the simulation time.

Second, it was assumed that the heat generation was uniform all over the battery. It was implemented as a time dependent heat source as where the input was the

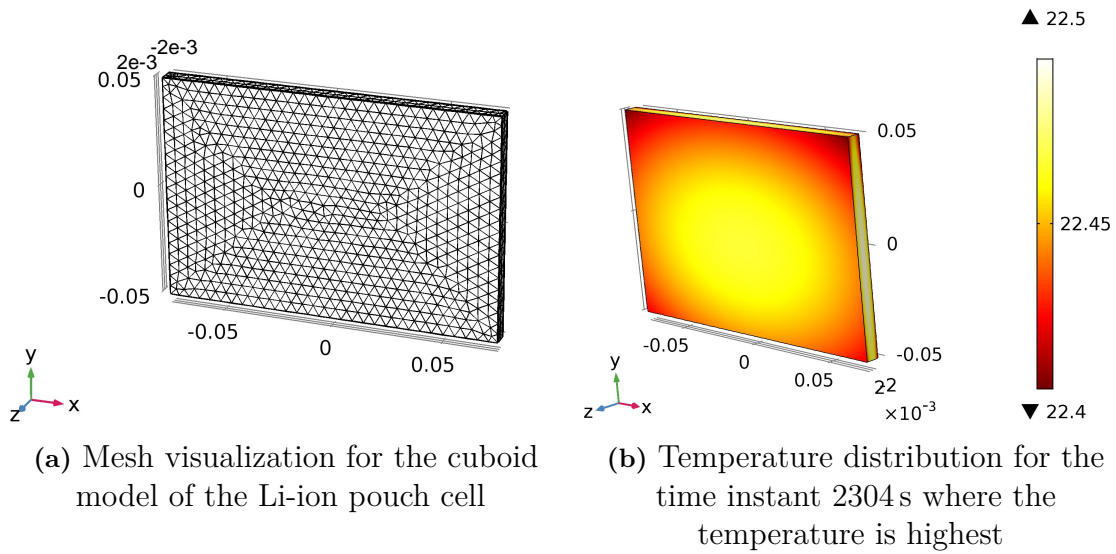


Figure 7.12: Mesh and temperature distribution for the COMSOL model of the pouch cell.

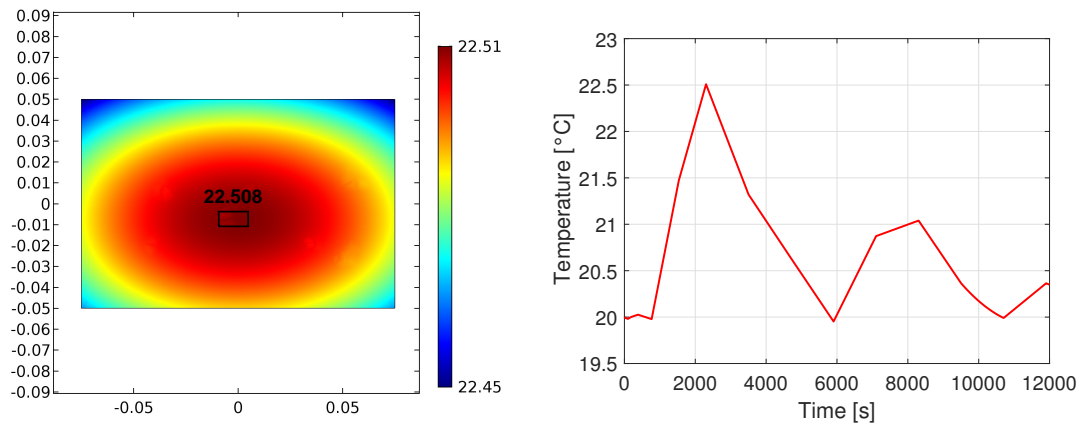
measured heat generation from the different load cycles. Last, the heat transfer was simplified by assuming that the cuboid was hanging in the air surrounded by a constant temperature of 273.15 K. Thus, natural convection was defined for the four vertical walls, the top portion and the bottom side. Radiation from the battery was also implemented where the thermal diffusivity was set to 0.9 as the surfaces are considered "shiny". Relevant settings and data are summarized in Table 7.9

Table 7.9: Parameters for the COMSOL model of the pouch cell

Parameters	Value
C_p	1091 [J kg ⁻¹ K ⁻¹]
Weight	0.238 [kg]
Height; Width; Thickness	100; 150; 6.67 [mm]
k_y ; k_x ; k_z	23; 31.4; 0.735 [W kg ⁻¹ K ⁻¹]
Mesh statistics	
Minimum element quality	0.3375
Average element quality	0.7884
Number of elements	9453
Study	
Time dependent	(0,0.5,12000) [s]
Heat transfer - radiation	
Emissivity (ϵ)	0.9 [m ² s ⁻¹]

7.6.1 Load cycle - 1.67C discharge and charge

The simulation was conducted for the 1.67C discharge and charge cycle with input from the generated heat (τ -corrected) presented in section 7.4. In Figure 7.12b the temperature distribution for the pouch cell model is visualized for the time instant (2304s) where the temperature is the highest.



(a) Temperature distribution of a xy-plane through the middle of the pouch cell.

(b) Temperature plot of the temperature for the hot-spot of the pouch cell.

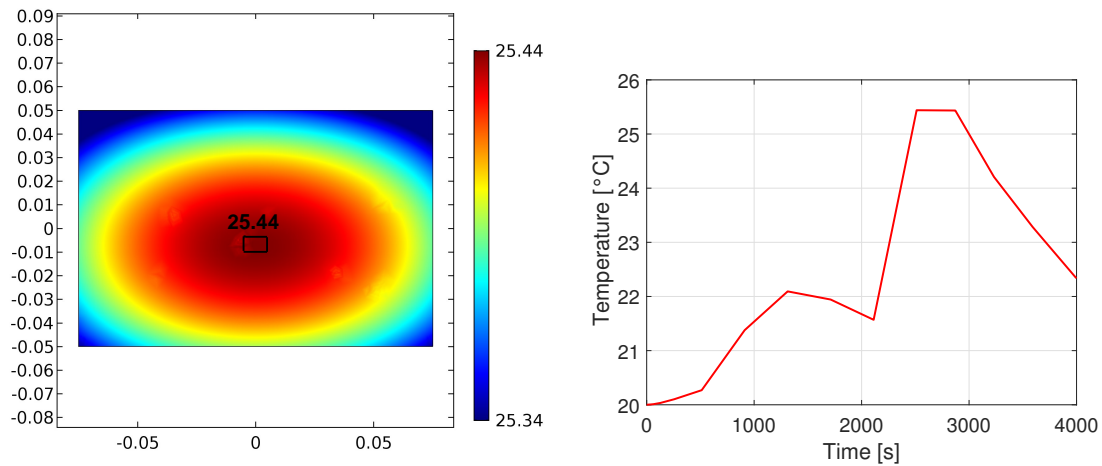
Figure 7.13: Temperature distributions both for a xy-plane through the middle of the cell and the temperature plot of a cut-point placed at the battery hot-spot.

This time instant was retrieved by evaluating the whole volume for maximum temperature over time. The highest temperature was found to be 22.508 °C for a cut-plane in xy-direction through the center of the cell. It can be seen in Figure 7.13b that the maximum temperature is not found in the mid point of this cut-plane which can be explained by the different natural convection defined in the simulation. However, this is most certainly the case for a real pouch cell as well since the terminals and stacked layers increase the complexity of the geometry. It is also evident that the high conductivity in the plane (x- and y-direction) distributes the heat very well which results in a low gradient over the surface plane. However, the absolute temperature results of the simulation was highly dependent on the heat transfer from the solid (convection and radiation) and only indicates distributions and hot-spots.

7.6.2 Load cycle - dynamic

In addition to the constant discharge and charge cycle a dynamic cycle was utilized for the pouch cell. The input for the COMSOL cuboid model was now the Tian-corrected heat generation from the dynamic cycle described in section 7.4. The temperature distribution was similar to the 1.67C case which was visualized in Figure 7.12b but the maximum temperature was higher for the dynamic cycle. In Figure 7.14a the temperature distribution for a xy-plane through the middle of the pouch

cell can be seen with the hot-spot indicated. The higher internal temperature of $25.44\text{ }^{\circ}\text{C}$ at the time instant 2512 s is a result of the higher C-rate for the dynamic cycle. This maximum temperature is recorded in the final charge of the cycle where a C-rate of 5 C is applied for the pouch cell.



(a) Temperature distribution of a xy-plane through the middle of the pouch cell.

(b) Temperature plot of the temperature for the hot-spot of the pouch cell.

Figure 7.14: Temperature distributions both for a xy-plane through the middle of the cell and the temperature plot of a cut-point placed at the battery hot-spot.

8

Conclusion

The purpose of this thesis work was to develop experimental methods using a custom-made IHC which enable accurate measurement of the heat generation during charge and discharge for different current-rates and thermal characterization of Li-ion cells. The high sensitivity as well as the versatility of this specific type of IHC in relation to Li-ion cell characterization was demonstrated through this work.

In order to measure the through-plane conductivity the IHC was modified and the method validity was established for a reference material of acrylic glass with a conductivity of $0.19 \text{ W m}^{-1} \text{ K}^{-1}$. The test results showed an average error of 13 % from this reference value. The through-plane conductivity of the pouch cell was found to be around $0.73 \text{ W m}^{-1} \text{ K}^{-1}$. It is concluded that the results can be further improved by better insulation of the setup and an accurate temperature control on the cooling system. Moreover, the method was inapplicable for the prismatic cell due to its aluminum casing.

A modular setup for measurement of the in-plane conductivity was fabricated and the method was validated for a sample of $14.76 \text{ W m}^{-1} \text{ K}^{-1}$ with an average error of 0.9%. Significantly lower error was observed in these experiments as compared to the through-plane thermal conductivity by utilizing better insulation box and an isothermal bath equipment. The measured in-plane conductivity for the pouch cell was 23.0 and $31.4 \text{ W m}^{-1} \text{ K}^{-1}$ in y-direction and x-direction respectively. The thermal conductivity values are different, in contrast to the general assumption that it is similar for both planar directions.

The specific heat capacity measurement method was validated against a sample of aluminum with an error of 5.7% against its datasheet value. The issue of shifting baseline during the experiment was overcome by a method of connecting both baselines as per varying calorimeter surface temperature (pressure plate). The measured specific heat capacity of both pouch and prismatic cell was around $1000 \text{ J kg}^{-1} \text{ K}^{-1}$.

The heat generation measurements for the pouch and prismatic cell showed that the calorimeter was able to measure powers in the range between 10 mW and 30 W. However, it was not able to record the instantaneous power for fast transients even when applying the dynamic Tian-correction. Due to the high sensitivity of the setup the reversible heat was visible for low currents but in order to quantify it correctly more stable conditions has to be achieved. The setup has to be insulated much more

thoroughly to avoid shifted baseline as well as interfering noise.

A simulation model for the pouch cell in COMSOL multiphysics was utilized in order to observe the resulting inside temperatures for the different load cycles. It was concluded that the maximum temperatures were achieved during the discharge portion for the 1.67C cycle and the fast charge portion for the dynamic cycle. However, the simulations should be seen as indications and proof of concept rather than true values since it was a simple cuboid model with approximated emissivity.

The results of this thesis work will be significant in design strategies of the thermal management of Li-ion battery packs. This includes optimization of cooling capacity, prediction of peak internal temperatures of Li-ion cells during operation and designing cooling paths through the battery packs. Consequently, this will lead to safer operation of Li-ion battery packs as well as prolong their life time.

8.1 Future work

The work conducted in this thesis can be improved in several aspects. One or many of the listed suggestions below can be implemented to increase the accuracy and usability of the measurements or simply enable measurement on more cells.

- The insulation of the setup proved to be one of the main difficulties which emphasizes the construction of a practical and well insulated setup. Moreover, the experimentation time should be extended for all experiments so that proper baselines are achieved.
- Since the custom made IHC is limited in size an up-scaled version should be built in order to measure on larger cells.
- The dependency of thermal properties on temperature, cell SOC and SOH can be further studied. This will be helpful in understanding the behavior of cells and validation of electro-thermal models.
- The method of thermal conductivity measurement proposed here is based on measurement of external temperature and heat rate. This made measurements on prismatic cells inapplicable. A possible extension of the work can be done by conducting experiments on the internal jelly roll (cell without external casing). This would give a better value of thermal conductivity for prismatic cells.
- The Li-ion cells have been limited in this work to pouch and prismatic cell types, however cylindrical cells can be used in the provided IHC as well. This would require an additional cell holder which can be rectangular in external geometry but have an internal cylindrical bore where the cell can be mounted maintaining good thermal contact.

- The simulations conducted for the pouch cell were simplified with a cuboid and rough estimations of the outward heat transfer. In order to achieve results that are usable for designing cooling systems more detailed models should be constructed. In addition, the thermal model could be coupled with an electrical and/or a chemical model.

8. Conclusion

Bibliography

- [1] P. Golinska, *Environmental Issues in Automotive Industry*. Springer, 2014.
- [2] G. B. Raines, *Electric vehicles: technology, research and development*. Nova Science, 2009.
- [3] H. Berg, “Batteries for electric vehicles: Materials and electrochemistry helena berg -: Cambridge university press, 2015 250 pages, isbn 9781107085930,” *MRS Bulletin*, vol. 41, no. 11, 2016.
- [4] J. Sun, G. Wei, L. Pei, R. Lu, K. Song, C. Wu, and C. Zhu, “Online internal temperature estimation for lithium-ion batteries based on kalman filter,” *Energies*, vol. 8, no. 5, pp. 4400–4415, 2015.
- [5] G. Vertiz, M. Oyarbide, H. Macicior, O. Miguel, I. Cantero, P. F. de Arroiabe, and I. Ulacia, “Thermal characterization of large size lithium-ion pouch cell based on 1d electro-thermal model,” *Journal of Power Sources*, vol. 272, pp. 476 – 484, 2014.
- [6] K. Chen, G. Unsworth, and X. Li, “Measurements of heat generation in prismatic li-ion batteries,” *Journal of Power Sources*, vol. 261, pp. 28 – 37, 2014.
- [7] V. Vishwakarma and A. Jain, “Measurement of in-plane thermal conductivity and heat capacity of separator in li-ion cells using a transient {DC} heating method,” *Journal of Power Sources*, vol. 272, pp. 378 – 385, 2014.
- [8] S. J. Bazinski and X. Wang, “Experimental study on the influence of temperature and state-of-charge on the thermophysical properties of an {LFP} pouch cell,” *Journal of Power Sources*, vol. 293, pp. 283 – 291, 2015.
- [9] B. Löwen, S. Schulz, and J. Seippel, “Heat capacity measurement by calibration with dynamic correction of the calorimetric output signal of a thermopile heat conduction calorimeter,” *Thermochimica Acta*, vol. 235, no. 2, pp. 147 – 152, 1994.
- [10] L. C. Casals, B. A. García, F. Aguesse, and A. Iturrondobeitia, “Second life of electric vehicle batteries: relation between materials degradation and environmental impact,” *The International Journal of Life Cycle Assessment*, vol. 22, no. 1, pp. 82–93, 2017.
- [11] J. Barkenbus, “Electric vehicles: Climate saviors, or not?,” *Issues in Science*

- and Technology*, vol. 33, pp. 55–59, Winter 2017. Name - International Energy Agency; Copyright - Copyright Issues in Science and Technology Winter 2017; Document feature - Tables; Photographs; Last updated - 2017-03-17; CODEN - ISTEEL; SubjectsTermNotLitGenreText - United States–US.
- [12] IEEE, “Ieee code of ethics.” <http://www.ieee.org/about/corporate/governance/p7-8.html>. [Accessed 26 Jan, 2017].
- [13] D. Linden, *Handbook of Batteries*. Electrical engineering, McGraw-Hill, 1995.
- [14] J. Groot and C. tekniska högskola. Institutionen för energi och miljö, *State-of-health Estimation of Li-ion Batteries: Cycle Life Test Methods*. Department of Energy and Environment, Chalmers University of Technology, 2012.
- [15] T. Reddy, *Linden’s Handbook of Batteries, 4th Edition*. McGraw-Hill Education, 2010.
- [16] C. Mikolajczak, M. Kahn, K. White, and R. T. Long, *Lithium-ion batteries hazard and use assessment*. Springer Science & Business Media, 2012.
- [17] M. Einhorn, F. V. Conte, C. Kral, and J. Fleig, “Comparison, selection, and parameterization of electrical battery models for automotive applications,” *IEEE Transactions on Power Electronics*, vol. 28, pp. 1429–1437, March 2013.
- [18] T. L. Bergman and F. P. Incropera, “Introduction to heat transfer,” 2011.
- [19] W. Zielenkiewicz and E. Margas, *Theory of Calorimetry*. Hot Topics in Thermal Analysis and Calorimetry, Springer Netherlands, 2002.
- [20] W. Hemminger and G. Höhne, *Calorimetry: fundamentals and practice*. Verlag Chemie, 1984.
- [21] L. Wadsö, “Operational issues in isothermal calorimetry,” *Cement and Concrete Research*, vol. 40, no. 7, pp. 1129 – 1137, 2010.
- [22] A. Beezer, *Biological microcalorimetry*. Academic Press, 1980.
- [23] European Thermodynamics Limited, “Datasheet for gm250-127-14-10 thermoelectric generator module.” [http://www.eurothermodynamics.com/products/datasheets/7-GM200-127-14-10%20\(2\).pdf](http://www.eurothermodynamics.com/products/datasheets/7-GM200-127-14-10%20(2).pdf). [Accessed 03 April, 2017].
- [24] Gamry Instruments, Inc., “Reference 3000 potentiostat/galvanostat/zra operator’s manual.” <https://www.gamry.com/assets/Uploads/Reference-3000-Operators-Manual.pdf>, December 2015.
- [25] Julabo USA Inc, “Datasheet for julabo f25ma.” <http://www.julabo.com/sites/default/files/downloads/productdatasheets/EN-US/JULABO-F25-MA--9153625.pdf>. [Accessed 07 April, 2017].
- [26] PICO Technology, “Pt100 platinum resistance thermometers.” <https://www.picotech.com/library/application-note/pt100-platinum-resistance-thermometers>. [Accessed 24 March, 2017].

- [27] Pico technology, "Pt-104 data logger." <https://www.picotech.com/download/datasheets/usb-pt-104-data-sheet.pdf>, January 2017.
- [28] RS Components, "Rs pro silicon heater mat." <http://docs-europe.electrocomponents.com/webdocs/157f/0900766b8157fc6a.pdf>. [Accessed 5 March, 2017].
- [29] Zotefoams, "Zotec N." <http://www.zotefoams.com/product/zotek/zotek-n/>. [Accessed 20 Feb, 2017].
- [30] Lauda, "Operating instructions immersion thermostat e100." http://www.severnsaleslabequip.com/manual-PDFs/W%20Waterbaths/Stirred%20&%20Unstirred%20Baths/Lauda%20E100%20bath_Staredition_2010-06-18_Internet.pdf. [Accessed 31 March, 2017].
- [31] C.Y.Ho and T.K.Chu, "Electrical resistivity and thermal conductivity of nine selected aisi stainless steels." <http://http://www.inductor-jmag.ru/files/content/a129160.pdf>, 1977.
- [32] J. Taylor, *Introduction To Error Analysis: The Study of Uncertainties in Physical Measurements*. A series of books in physics, University Science Books, 1997.

A

Appendix 1

A.1 Measurement uncertainty - calibration coefficient

The theorem of uncertainty propagation was utilized for calculation as mentioned below [32].

Uncertainties in sums and differences:

Suppose that x, \dots, w are measured with uncertainty $\delta x, \dots, \delta w$ and the measured value used to compute

$$q = x + \dots + z - (u + \dots + w) \quad (\text{A.1})$$

If the uncertainties in x, \dots, w are known to be independent and random, then uncertainty in q is quadratic sum

$$\delta q = \sqrt{\delta x^2 + \dots + \delta z^2 + \delta u^2 + \dots + \delta w^2} \quad (\text{A.2})$$

Uncertainties in products and quotients:

Suppose that x, \dots, w are measured with uncertainty $\delta x, \dots, \delta w$ and the measured value used to compute

$$q = \frac{x \times \dots \times z}{u \times \dots \times w} \quad (\text{A.3})$$

If the uncertainties in x, \dots, w are known to be independent and random, then uncertainty in q is quadrature of original fractional uncertainties,

$$\frac{\delta q}{|q|} = \sqrt{\left(\frac{\delta x}{|x|}\right)^2 + \dots + \left(\frac{\delta z}{|z|}\right)^2 + \left(\frac{\delta u}{|u|}\right)^2 + \dots + \left(\frac{\delta w}{|w|}\right)^2} \quad (\text{A.4})$$

Sample calculation for measurement uncertainty evaluation in calibration coefficient ε at combined power of 1.65W for Calorimeter A side only:

The measurement of resistance was carried out by using FLUKE 787 device with measurement uncertainties as per Table 3.1.

Voltage divider:

Measured value of resistance $R1=23.99 \text{ k}\Omega$

A. Appendix 1

Uncertainty in R1 resistance $\delta R1 = (0.2\% \times 23.99 + 1 \times 0.01)\text{k}\Omega = 0.05798 \text{ k}\Omega$

Similarly for measured resistance $R2=51 \text{ k}\Omega$

Uncertainty in measurement $\delta R2 = (0.2\% \times 51 + 1 \times 0.1)\text{k}\Omega = 0.202 \text{ k}\Omega$

(higher resistance than 40 k Ω , hence resolution changes)

Sum $(R1+R2) = 74.99 \text{ k}\Omega$

As per (A.2) Uncertainty $\delta(R1 + R2) = \sqrt{0.05798^2 + 0.202^2} = 0.21016 \text{ k}\Omega$

Fraction $R_f = (R1 + R2)/R1 = 3.12588 \text{ k}\Omega$

As per (A.4), uncertainty $\delta R_f = 3.12588 \times \sqrt{\left(\frac{0.21016}{74.99}\right)^2 + \left(\frac{0.05798}{23.99}\right)^2} = 0.01156 \text{ k}\Omega$

Measurement of Voltage was carried out by GAMRY with measurement uncertainty as per Table 3.1.

Measured heater voltage $V_m = 0.88204 \text{ V}$

Uncertainty $\delta V_m = (0.2\% \times 0.88204 + 0.001) = 0.00276 \text{ V}$

Actual Heater voltage $V_h = V_m \times R_f = 2.75718 \text{ V}$

As per (A.4) $\delta V_h = 2.75718 \times \sqrt{\left(\frac{0.00276}{0.88204}\right)^2 + \left(\frac{0.01156}{3.12588}\right)^2} = 0.01337 \text{ k}\Omega$

Measurement of current was carried out by GAMRY with measurement uncertainty as per Table 3.1.

Current through heater $I = 0.299037 \text{ A}$

Uncertainty $\delta I = 0.2\% \times 0.299037 + (5e - 15) + 0.05\% \times 3 = 0.00209 \text{ A}$

Power applied to heaters $P = V_h \times I = 0.82449 \text{ W}$

As per (A.4), uncertainty in power $\delta P = 0.82449 \times \sqrt{\left(\frac{0.01337}{2.75718}\right)^2 + \left(\frac{0.00209}{0.299037}\right)^2} = 0.004405 \text{ W}$

Measured Heat flow sensor voltage $U = 0.046706 \text{ V}$

As per Table 3.1, uncertainty $\delta U = 0.00109 \text{ V}$

Calibration coefficient $\varepsilon = \frac{P}{U} = 17.653 \text{ W V}^{-1}$

Uncertainty in coefficient $\delta\varepsilon = 17.653 \times \sqrt{\left(\frac{0.004405}{0.82449}\right)^2 + \left(\frac{0.00109}{0.046706}\right)^2} = 0.423880457 \text{ W V}^{-1} = 2.4\%$

A.2 Measurement uncertainty - through-plane thermal conductivity

The theorem of uncertainty propagation [32] was utilized for calculation of uncertainty in the through-plane conductivity measurements.

A sample calculation is shown below for through plane conductivity measurement for acrylic sheet with power level of 2.21 W through the sample.

Measurement of temperature was carried out by using PICO device which has measurement uncertainty as per Table 3.1.

Measured temperature on sample hot side $T_h = 21.13225\text{ }^\circ\text{C}$

Uncertainty $\delta T_h = (0.01\% \times 21.13225 + 0.015) = 0.01711\text{ }^\circ\text{C}$

Measured temperature on sample cold side $T_c = 19.58243\text{ }^\circ\text{C}$

Uncertainty $\delta T_c = (0.01\% \times 19.58243 + 0.015) = 0.01695\text{ }^\circ\text{C}$

Difference in temperature across the sample $T_{diff} = T_h - T_c = 1.54982\text{ }^\circ\text{C}$

As per (A.2), uncertainty $\delta T_{diff} = \sqrt{0.01711^2 + 0.01695^2} = 0.02409\text{ }^\circ\text{C}$

Length measurement was carried out by digital vernier calipers with uncertainty in measurement as per Table 3.1.

Measured thickness of sample $L = 2\text{ mm}$

Uncertainty in thickness $\delta L = 0.02\text{ mm}$

Measured width of sample $L_1 = 151.48\text{ mm}$

Uncertainty in thickness $\delta L_1 = 0.02\text{ mm}$

Measured length of sample $L_2 = 99.15\text{ mm}$

Uncertainty in thickness $\delta L_2 = 0.02\text{ mm}$

Area of sample $A = L_1 \times L_2 = 15019.242\text{ mm}^2$

As per (A.4), uncertainty in area $\delta A = 15019.242 \times \sqrt{\left(\frac{0.02}{151.48}\right)^2 + \left(\frac{0.02}{99.15}\right)^2} = 3.62087\text{ mm}^2$

Sensor voltage was measured using GAMRY which has measurement uncertainty as per Table 3.1.

Measured sensor baseline voltage $U_0 = 0.00424\text{ V}$

Uncertainty in sensor baseline $\delta U_0 = (0.2\% \times 0.00424 + 0.001) = 0.00101\text{ V}$

Measured sensor voltage $U_m = 0.12955 \text{ V}$

Uncertainty in sensor voltage $\delta U_m = (0.2\% \times 0.12955 + 0.001) = 0.00126 \text{ V}$

Steady state voltage $U_s = U_m - U_0 = 0.12531 \text{ V}$

As per (A.2), uncertainty in steady state voltage $\delta U_s = \sqrt{0.00101^2 + 0.00126^2} = 0.00161 \text{ V}$

Calibration coefficient for calorimeter A $\varepsilon = 17.6048 \text{ W V}^{-1}$

Uncertainty in coefficient $\delta\varepsilon = 2.4\% \times 17.6048 = 0.42283 \text{ W V}^{-1}$

Heat flow rate $Q = \varepsilon \times U_s = 2.20606 \text{ W}$

As per (A.4), uncertainty $\delta Q = 2.20606 \times \sqrt{\left(\frac{0.00161}{0.12531}\right)^2 + \left(\frac{0.42283}{17.6048}\right)^2} = 0.060117 \text{ W}$

Product $(QL) = Q \times L = 0.004412$

Uncertainty $\delta(QL) = 0.004412 \times \sqrt{\left(\frac{0.060117}{2.20606}\right)^2 + \left(\frac{0.02}{2}\right)^2} = 0.000128$

Product $(AT_{diff}) = A \times T_{diff} = 0.02327$

Uncertainty $\delta(AT_{diff}) = 0.02327 \times \sqrt{\left(\frac{3.62087}{15019.242}\right)^2 + \left(\frac{0.02409}{1.54982}\right)^2} = 0.000362$

Through-plane conductivity $k_z = (QL)/(AT_{diff}) = 0.18954 \text{ W m}^{-1} \text{ K}^{-1}$

Uncertainty $\delta k_z = 0.18954 \times \sqrt{\left(\frac{0.000128}{0.004412}\right)^2 + \left(\frac{0.000362}{0.02327}\right)^2} = 0.006241 \text{ W m}^{-1} \text{ K}^{-1} = 3.3\%$

A.3 Measurement uncertainty - in-plane thermal conductivity

The theorem of uncertainty propagation [32] was utilized for calculation of uncertainty in the specific heat capacity measurements.

A sample calculation is shown below for in plane conductivity measurement for Stainless Steel sample with power level of 1.32 W through the sample.

Measurement of temperature was carried out by using PICO device which has measurement uncertainty as per Table 3.1.

Measured temperature on sample cold side $T_h = 22.235 \text{ }^\circ\text{C}$

Uncertainty $\delta T_c = (0.01\% \times 22.235 + 0.015) = 0.0172 \text{ }^\circ\text{C}$

Measured temperature on sample hot side $T_c = 24.939\text{ }^\circ\text{C}$

Uncertainty $\delta T_h = (0.01\% \times 24.939 + 0.015) = 0.0174\text{ }^\circ\text{C}$

Baseline temperature difference $T_0 = 0.202\text{ }^\circ\text{C}$

Uncertainty $\delta T_0 = (0.01\% \times 0.202 + 0.015) = 0.0150\text{ }^\circ\text{C}$

Difference in temperature across the sample $T_{diff} = T_h - T_c = 2.50\text{ }^\circ\text{C}$

As per (A.2), uncertainty $\delta T_{diff} = \sqrt{0.01711^2 + 0.01695^2 + 0.015^2} = 0.0287\text{ }^\circ\text{C}$

Length measurement was carried out by digital vernier calipers with uncertainty in measurement as per Table 3.1.

Measured thickness of sample $L_1 = 2\text{ mm}$

Uncertainty in thickness $\delta L = 0.02\text{ mm}$

Measured width of sample $L_2 = 151.04\text{ mm}$

Uncertainty in thickness $\delta L_1 = 0.02\text{ mm}$

Measured length of sample $L = 20\text{ mm}$

Uncertainty in thickness $\delta L_2 = 0.02\text{ mm}$

Area of sample $A = L_1 \times L_2 = 302.084\text{ mm}^2$

As per (A.4) Uncertainty in area $\delta A = 302.084 \times \sqrt{\left(\frac{0.02}{151.04}\right)^2 + \left(\frac{0.02}{2}\right)^2} = 3.021\text{ mm}^2$

Sensor voltage was measured using GAMRY which has measurement uncertainty as per Table 3.1.

Measured sensor baseline voltage $U_0 = 0.00103\text{ V}$

Uncertainty in sensor baseline $\delta U_0 = (0.2\% \times 0.00103 + 0.001) = 0.001002\text{ V}$

Measured sensor voltage $U_m = 0.0324\text{ V}$

Uncertainty in sensor voltage $\delta U_m = (0.2\% \times 0.0324 + 0.001) = 0.00106\text{ V}$

Steady state voltage $U_s = U_m - U_0 = 0.0314\text{ V}$

As per (A.2), uncertainty in steady state voltage $\delta U_s = \sqrt{0.00106^2 + 0.001002^2} = 0.00146\text{ V}$

Calibration coefficient for heat flow sensors $\varepsilon = 17.382\text{ W V}^{-1}$

Uncertainty in coefficient $\delta \varepsilon = 2.4\% \times 17.382 = 0.4174\text{ W V}^{-1}$

Heat flow rate $Q = \varepsilon \times U_s = 0.546 \text{ W}$

As per (A.4) Uncertainty $\delta Q = 0.546 \times \sqrt{\left(\frac{0.00146}{0.0314}\right)^2 + \left(\frac{0.4174}{17.6048}\right)^2} = 0.0286 \text{ W}$

Product $(QL) = Q \times L = 0.0109$

Uncertainty $\delta(QL) = 0.0109 \times \sqrt{\left(\frac{0.0286}{0.546}\right)^2 + \left(\frac{0.02}{20}\right)^2} = 0.000572$

Product $(AT_{diff}) = A \times T_{diff} = 0.000755$

Uncertainty $\delta(AT_{diff}) = 0.000755 \times \sqrt{\left(\frac{3.0211}{302.084}\right)^2 + \left(\frac{0.0287}{2.5}\right)^2} = 1.1518E - 05$

In-plane conductivity $k_y = (QL)/(AT_{diff}) = 14.474 \text{ W m}^{-1} \text{ K}^{-1}$

Uncertainty $\delta k_y = 14.474 \times \sqrt{\left(\frac{0.000572}{0.0109}\right)^2 + \left(\frac{1.1518E-05}{0.000755}\right)^2} = 0.789063409 \text{ W m}^{-1} \text{ K}^{-1} = 5.4\%$

A.4 Measurement uncertainty - specific heat capacity

The theorem of uncertainty propagation was utilized [32] for calculation of uncertainty in specific heat capacity measurement.

A sample calculation is shown below for specific heat capacity measurement of an aluminum sample.

Measurement of temperature was carried out by using PICO device which has measurement uncertainty as per Table 3.1.

Measured initial temperature of sample $T_i = 19.898 \text{ }^\circ\text{C}$

Uncertainty $\delta T_i = (0.01\% \times 19.898 + 0.015) = 0.01704 \text{ }^\circ\text{C}$

Measured final temperature of sample $T_f = 21.788 \text{ }^\circ\text{C}$

Uncertainty $\delta T_f = (0.01\% \times 21.788 + 0.015) = 0.01733 \text{ }^\circ\text{C}$

Difference in temperature $T_{diff} = T_f - T_i = 1.889 \text{ }^\circ\text{C}$

As per (A.2), uncertainty $\delta T_{diff} = \sqrt{0.01704^2 + 0.01733^2} = 0.0243 \text{ }^\circ\text{C}$

Mass measurement was done by Mettler PC440 with uncertainty in measurement of $\pm 50 \text{ mg}$ for mass between 0-420 g.

Measured mass of sample $m = 0.11579 \text{ kg}$

Uncertainty in mass $\delta m = 0.00005 \text{ kg}$

Sensor voltage was measured using GAMRY which has measurement uncertainty as per Table 3.1.

Net integrated area under curve $V_{net} = 11.796 \text{ V s}$

Uncertainty $\delta V_{net} = (0.2\% \times 11.796 + 0.001) = 0.0246 \text{ V s}$

Calibration coefficient for heat flow sensors $\varepsilon = 17.6048 \text{ W V}^{-1}$

Uncertainty in coefficient $\delta\varepsilon = 2.4\% \times 17.6048 = 0.42284 \text{ W V}^{-1}$

Heat flow absorbed $E_{net} = \varepsilon \times V_{net} = 207.67 \text{ J}$

As per (A.4), uncertainty $\delta Q = 207.67 \times \sqrt{\left(\frac{0.42284}{17.6048}\right)^2 + \left(\frac{0.0246}{11.796}\right)^2} = 5.0067 \text{ J}$

Product $(mT_{diff}) = m \times T_{diff} = 0.218$

Uncertainty $\delta(AT_{diff}) = 0.218 \times \sqrt{\left(\frac{0.00005}{0.11579}\right)^2 + \left(\frac{0.0243}{1.889}\right)^2} = 0.00281$

Specific heat capacity $C_p = (QL)/(AT_{diff}) = 949.1 \text{ J kg}^{-1} \text{ K}^{-1}$

Uncertainty $\delta C_p = 949.1 \times \sqrt{\left(\frac{0.00281}{0.218}\right)^2 + \left(\frac{5.0067}{207.67}\right)^2} = 25.938 \text{ J kg}^{-1} \text{ K}^{-1} = 2.7\%$